

| | | | | | |
|---|--|---|---|--|-----------|
| 1. Report No. FHWA/TX-07/0-4642-3 | | 2. Government Accession No. | | 3. Recipient's Catalog No. | |
| 4. Title and Subtitle CALCULATION OF AREAL REDUCTION FACTORS USING NEXRAD PRECIPITATION ESTIMATES | | | | 5. Report Date October 2005 Published: November 2006 | |
| | | | | 6. Performing Organization Code | |
| 7. Author(s) Francisco Olivera, Dongkyun Kim, Janghwoan Choi and Ming-Han Li | | | | 8. Performing Organization Report No. Report 0-4642-3 | |
| 9. Performing Organization Name and Address Texas Transportation Institute The Texas A&M University System College Station, Texas 77843-3135 | | | | 10. Work Unit No. (TRAIS) | |
| | | | | 11. Contract or Grant No. Project 0-4642 | |
| 12. Sponsoring Agency Name and Address Texas Department of Transportation Research and Technology Implementation Office P.O. Box 5080 Austin, Texas 78763-5080 | | | | 13. Type of Report and Period Covered Technical Report: September 2003 - August 2005 | |
| | | | | 14. Sponsoring Agency Code | |
| 15. Supplementary Notes Project performed in cooperation with the Texas Department of Transportation and the Federal Highway Administration. Project Title: GIS Static Storm Model Development URL: http://tti.tamu.edu/document/0-4642-3.pdf | | | | | |
| 16. Abstract In general, larger catchments are less likely than smaller catchments to experience high intensity storms over the whole of the catchment area. Therefore, the conversion of point precipitation into area-averaged precipitation is necessary whenever an area, large enough for rainfall not to be uniform, is to be modeled. However, while point precipitation has been well recorded because of the availability of rain gauge data, areal precipitation cannot be measured, and its estimation has been a subject of research for the last decades. With the understanding that the <i>Next Generation Radar</i> (NEXRAD) precipitation data distributed by the U.S. National Weather Service (NWS) are the best data with spatial coverage available for large areas, this report addresses the estimation of areal reduction factors (ARFs) using this type of data. The study site is the 685,000-km ² area of the state of Texas. Storms were assumed to be elliptically shaped of different aspect ratios and orientations. It was found that, in addition to the storm duration and area already considered in previous studies, ARFs depend also on the geographic region and the precipitation depth, which is associated with the storm frequency for a given duration. Researchers also studied storm shape and orientation. | | | | | |
| 17. Key Words Precipitation, Areal Reduction Factors, Geographic Information Systems (GIS), NEXRAD Precipitation Estimates, Texas | | | 18. Distribution Statement No restrictions. This document is available to the public through NTIS: National Technical Information Service Springfield, Virginia 22161 http://www.ntis.gov | | |
| 19. Security Classif.(of this report) Unclassified | | 20. Security Classif.(of this page) Unclassified | | 21. No. of Pages 84 | 22. Price |

CALCULATION OF AREAL REDUCTION FACTORS USING NEXRAD PRECIPITATION ESTIMATES

by

Francisco Olivera, Ph.D., P.E.
Assistant Professor
Department of Civil Engineering

Dongkyun Kim
Graduate Assistant – Research
Department of Civil Engineering

Janghwoan Choi
Graduate Assistant – Research
Department of Civil Engineering

and

Ming-Han Li, Ph.D.
Assistant Professor
Department of Landscape Architecture and Urban Planning

Report 0-4642-3
Project 0-4642
Project Title: GIS Static Storm Model Development

Performed in cooperation with the
Texas Department of Transportation
and the
Federal Highway Administration

October 2005
Published: November 2006

TEXAS TRANSPORTATION INSTITUTE
The Texas A&M University System
College Station, Texas 77843-3135

DISCLAIMER

This research was performed in cooperation with the Texas Department of Transportation (TxDOT) and the Federal Highway Administration (FHWA). The contents of this report reflect the views of the authors, who are responsible for the facts and the accuracy of the data presented herein. The contents do not necessarily reflect the official view or policies of the FHWA or TxDOT. This report does not constitute a standard, specification, or regulation.

This report is not intended for construction, bidding, or permits purposes. The engineer in charge of the project was Francisco Olivera, P.E. #88213.

The United States Government and the State of Texas do not endorse products or manufacturers. Trade or manufacturers' names appear herein solely because they are considered essential to the object of this report.

ACKNOWLEDGMENTS

This project was conducted in cooperation with TxDOT and FHWA.

The authors would like to thank Project Director Rose Marie Klee, Project Coordinator David Stolpa, and Project Advisors Tedd Carter, George Herrmann, Amy Ronnfeldt, Jaime Villena-Morales and David Zwernemann for their input and support during this project.

TABLE OF CONTENTS

| | Page |
|-------------------------------------|-------------|
| List of Figures..... | viii |
| List of Tables | x |
| 1. Introduction..... | 1 |
| 2. Precipitation Data | 7 |
| 3. Methodology | 13 |
| 4. Results and Analysis | 17 |
| 5. ArcGIS_Storm Documentation | 35 |
| 6. Moving Storms | 61 |
| 7. Conclusions..... | 69 |
| 8. References..... | 71 |

LIST OF FIGURES

| | Page |
|---|-------------|
| Figure 2.1: Texas WSR-88D Radars (Source: U.S. National Weather Service, http://www.roc.noaa.gov/interactive/defaultIE.asp)..... | 8 |
| Figure 2.2: Scanning Domain of the Radars within and around Texas. Red Points: Radar Locations; Blue Area: Radar Scanning Domain; and Black Outline: Texas Border..... | 8 |
| Figure 2.3: Area Served by the West Gulf River Forecasting Center (Purple) and HRAP Grid Extent in Which the Data Are Distributed (Green)..... | 11 |
| Figure 3.1: West Gulf River Forecasting Center HRAP Grid..... | 13 |
| Figure 3.2: 50 km Buffer around Texas..... | 13 |
| Figure 3.3: 1-hr Duration Concurrent Precipitation Field for June 4, 2003, at 6:00 am. The Color of Each Cell Represents the Precipitation Depth. Red Cells Have Higher Precipitation Depth than the Blue Ones..... | 14 |
| Figure 3.4: Location of the Cells for Which ARFs Were Calculated for a Storm Duration of 1 hr and Using Stage III Data of 2003..... | 15 |
| Figure 3.5: Ellipses of Different Areas Shown on a Precipitation Field. Each Ellipse Has Its Own Aspect and Inclination Angle..... | 16 |
| Figure 4.1: Effect of Location on the ARF Values..... | 17 |
| Figure 4.2: Effect of Precipitation Depth on the ARF Values..... | 18 |
| Figure 4.3: Regions of Texas (U.S. Geological Survey 1998)..... | 18 |
| Figure 4.4: ARF-Area Plot for Region 4 and Storm Duration of 24. Note the Scatter of the Points around the Mean Line, Which Is Presumed to Be Caused by the Differences in Precipitation Depth..... | 19 |
| Figure 4.5: ARF-Area Plot for Region 4 and Duration of 24 hrs..... | 26 |
| Figure 4.6: ARF-Area Plot for Region 4, Duration of 24 hrs and Depth between 64 mm and 102 mm..... | 26 |
| Figure 4.7a: Normalized Histograms of Aspect for a Duration of 1 hr..... | 27 |
| Figure 4.7b: Normalized Histograms of Aspect for a Duration of 3 hrs..... | 28 |
| Figure 4.7c: Normalized Histograms of Aspect for a Duration of 6 hrs..... | 28 |
| Figure 4.7d: Normalized Histograms of Aspect for a Duration of 12 hrs..... | 29 |
| Figure 4.7e: Normalized Histograms of Aspect for a Duration of 24 hrs..... | 29 |
| Figure 4.8a: Normalized Histograms of Angle for a Duration of 1 hr..... | 30 |
| Figure 4.8b: Normalized Histograms of Angle for a Duration of 3 hrs..... | 30 |
| Figure 4.8c: Normalized Histograms of Angle for a Duration of 6 hrs..... | 31 |
| Figure 4.8d: Normalized Histograms of Angle for a Duration of 12 hrs..... | 31 |
| Figure 4.8e: Normalized Histograms of Angle for a Duration of 24 hrs..... | 32 |
| Figure 4.9: Comparison of ARF-Area Curves According to Different Studies..... | 33 |
| Figure 5.1: ArcGIS_Storm Toolbar..... | 35 |
| Figure 5.2: Project Working Directory Menu..... | 35 |
| Figure 5.3: The Project Set Up Window..... | 36 |
| Figure 5.4: Project Folder Window..... | 36 |
| Figure 5.5: Climate Region Frame..... | 36 |
| Figure 5.6: Open Feature Class of Climate Region for Texas..... | 37 |
| Figure 5.7: Select Watersheds Menu..... | 37 |
| Figure 5.8: Select Watersheds Window..... | 38 |

| | |
|---|----|
| Figure 5.9: Example of Selecting Watersheds..... | 38 |
| Figure 5.10: Hypothetical Storm Menu..... | 39 |
| Figure 5.11: Hypothetical/FHS Menu..... | 40 |
| Figure 5.12: Input Storm Properties Window..... | 40 |
| Figure 5.13: Storm Properties Window..... | 41 |
| Figure 5.14: IDF Curves Window..... | 41 |
| Figure 5.15: Edit IDF Curves Window..... | 42 |
| Figure 5.16: Edit Durations Window..... | 43 |
| Figure 5.17: Edit Isohyet Area Window..... | 44 |
| Figure 5.18: Develop Storm Menu..... | 44 |
| Figure 5.19: Developing Storm Window..... | 45 |
| Figure 5.20: Symbology Setup..... | 45 |
| Figure 5.21: Storm Feature Class Table..... | 46 |
| Figure 5.22: PMP Menu..... | 47 |
| Figure 5.23: PMP Project Setup Menu..... | 47 |
| Figure 5.24: PMP Project Setup Window..... | 48 |
| Figure 5.25: Location of the HMR52 Executable File..... | 48 |
| Figure 5.26: Location of the PMP Geodatabase..... | 49 |
| Figure 5.27: Input and Output File for HMR52..... | 49 |
| Figure 5.28: Prepare Storm Inputs Menu..... | 50 |
| Figure 5.29: Input Data Window..... | 50 |
| Figure 5.30: Edit Durations Window..... | 52 |
| Figure 5.31: Edit Isohyet Areas Window..... | 53 |
| Figure 5.32: Basin Table..... | 53 |
| Figure 5.33: Run HMR52 Menu..... | 54 |
| Figure 5.34: Execute HMR52 Window..... | 55 |
| Figure 5.35: HMR52 DOS Window..... | 55 |
| Figure 5.36: Develop Storm Menu..... | 56 |
| Figure 5.37: Developing Storm Window..... | 56 |
| Figure 5.38: PMP Storm..... | 57 |
| Figure 5.39: PMP Storm Table..... | 58 |
| Figure 5.40: Modified PMP Menu..... | 58 |
| Figure 5.41: Animation Toolbar..... | 59 |
| Figure 5.42: Animation Setup Window..... | 59 |
| Figure 6.1: Aspects of Frontal Rainstorms (Mellor 1996)..... | 62 |
| Figure 6.2: Storm Analysis..... | 63 |
| Figure 6.3: Image Process by the Sobel Method..... | 64 |
| Figure 6.4: Image Process by Eliminating Noise..... | 64 |
| Figure 6.5: Image Process Using the Canny Algorithm..... | 65 |
| Figure 6.6: Segmentation by a Contour Line..... | 65 |
| Figure 6.7: Labeled Objects..... | 66 |
| Figure 6.8: Mesoscale Convective Systems or Rain Bands (Longest Dimension > 100 km). | 66 |
| Figure 6.9: Multicell Storms or Rain Cluster (Longest Dimension < 100 km). | 67 |
| Figure 6.10: Rain Cells (Longest Dimension \approx 5 km). | 67 |
| Figure 6.11: Storm Data Model..... | 68 |

LIST OF TABLES

| | Page |
|---|-------------|
| Table 3.1: Number of Cells for Which ARFs Were Calculated. | 15 |
| Table 4.1: a, b and c for a Duration of 1 hr..... | 21 |
| Table 4.2: a, b and c for a Duration of 3 hrs. | 22 |
| Table 4.3: a, b and c for a Duration of 6 hrs. | 23 |
| Table 4.4: a, b and c for a Duration of 12 hrs. | 24 |
| Table 4.5: a, b and c for a Duration of 24 hrs. | 25 |

1. INTRODUCTION

In general, “larger catchments are less likely than smaller catchments to experience high intensity storms over the whole of the catchment area” (Siriwardena and Weinmann 1996). Therefore, the conversion of point precipitation into area-averaged precipitation is necessary whenever an area, large enough for rainfall not to be uniform, is to be modeled. However, while point precipitation has been well studied because of the availability of rain gauge data, areal precipitation cannot be measured, and its estimation has been a subject of research for the last few decades (U.S. Weather Bureau 1957, 1958a, 1958b, 1959, 1960, 1964; Rodriguez-Iturbe and Mejia 1974; Frederick et al. 1977; Omolayo 1993; Srikathan 1995; Bacchi and Ranzi 1996; Siriwardena and Weinmann 1996; Sivapalan and Blöschl 1998; Asquith and Famiglietti 2000; De Michele et al. 2001; Durrans et al. 2002). This report discusses the estimation of the ratios of areal average precipitation to point precipitation – also called areal reduction factors (ARFs) – using radar precipitation data. The study site is the 685,000-km² area covered by the state of Texas in the United States.

With the understanding that the *Next Generation Radar* (NEXRAD) data, the radar precipitation data distributed by the United States National Weather Service (NWS), are the best data with areal coverage in Texas, this report addresses the conversion of point precipitation into areal precipitation using these radar data. It was found that, in addition to the storm duration and area already considered in previous studies, ARFs depend on the precipitation depth and region where the event takes place.

A number of approaches for converting point precipitation into areal precipitation are based on observed precipitation data. Traditionally, ARF-estimation algorithms have been grouped under two broad categories: those based on geographically fixed rain gauge networks (known as geographically fixed ARFs) and those based on individual storm events (known as storm-centered ARFs) (Srikathan 1995). The geographically fixed approach is particularly suited for using discrete (i.e., point) precipitation data, and ARFs are calculated using data of rain gauge networks. ARFs are calculated as the ratio of a representative precipitation depth over the area covered by the network to a (not necessarily concurrent) representative point precipitation depth. How to estimate the area covered by the network, the representative precipitation depth over the area, or the representative point precipitation depth, however, changes from method to method. Moreover, based on the algorithms used to calculate geographically fixed ARFs, it can

be said that they are sensitive to the configuration of the network (i.e., adding or removing a rain gauge can affect the ARF values), and that they do not consider concurrent precipitation depths (i.e., the areal and point precipitation do not correspond necessarily to the same event). The storm-centered approach, on the other hand, is well suited for using continuous (i.e., surface) precipitation data, such as radar data. In this case, ARFs are calculated for individual events for which they describe their areal properties, and are equal to the ratio of the average precipitation depth over an area to the concurrent point precipitation depth in the storm center. Because storm-centered ARFs are estimated for individual events, they can capture the anisotropy of the rainfall field (i.e., the storm shape and orientation) and the seasonal effect of the atmospheric processes. The storm-centered approach, however, has the disadvantage that the ARFs are “applicable to specific types of storm events” (Srikathan 1995), and, therefore, unless a large sample of storm-centered ARF values are estimated, the main and seasonal trends in the area might not be captured. In general, it can be observed that while geographically fixed ARFs are the result of statistically processing precipitation data and then calculating ARF values, storm-centered ARFs are the result of calculating ARF values for each of a large sample of storms and then statistically processing them. Both approaches have strengths and weaknesses, and, in both cases, the extrapolation to areas different from those for which the ARFs were derived should be done carefully. Other approaches for calculating ARFs do exist, which, in a way, indicate the complexity of the problem.

One of the first attempts at estimating ARFs in the United States was documented in Technical Paper 29 – Parts 1 to 5, frequently referred to as TP-29 (U.S. Weather Bureau 1957, 1958a, 1958b, 1959, 1960). In TP-29, for the area associated with a precipitation gauge network, the ARF values are estimated using the equation $ARF = k \frac{\sum_{j=1}^n \bar{P}_j}{\sum_{j=1}^n \sum_{i=1}^k P_{ij}}$, where \bar{P}_j [L] is the annual maximum areal precipitation in year j, P_{ij} [L] is the annual maximum point precipitation at gauge i in year j, k is the number of rain gauges in the network, and n is the number of years considered in the calculations. The area is defined by k circles of diameter equal to the average gauge spacing. The analysis was conducted for only 20 rain gauge networks – 13 of which were located in the Midwest and eastern United States, and 7 along the Pacific Coast – and for periods of record ranging from 5 to 16 years. ARFs for storm durations of 0.5, 1, 3, 6 and 24 hrs and areas up to approximately 1,000 km², were estimated. Because of the averaging of the areal and

point precipitations, the resulting factors correspond to a 2.3-year return period. Moreover, according to TP-29, ARFs do not depend on geographic location, which implies that the same values apply for all storms regardless of the local climate conditions. To summarize all the TP-29 curves, [Eagleson \(1972\)](#) suggested $ARF = 1 - \exp(-1.1t_d^{0.25}) + \exp(-1.1t_d^{0.25} - 0.026A)$, where t_d is the storm duration (hours) and A is the area (km^2). Likewise, in Technical Paper 49 (i.e., TP-49) ([U.S. Weather Bureau 1964](#)), the relationship between the ARFs and the storm recurrence intervals was studied for 2-, 5-, 10-, 25- and 100-year events of durations of 24 and 48 hrs. It was concluded that ARFs are not affected by the precipitation recurrence interval. Additionally, because of the insufficient precipitation data, no clear indication was found to relate ARFs to geographic location.

Likewise, as part of an effort for calculating ARFs for the region of Victoria, Australia, [Srikathan \(1995\)](#) conducted a thorough literature review of the methods available for converting point to area precipitation. As part of the same project, [Siriwardena and Weinmann \(1996\)](#) estimated ARF values based on daily rainfall data from over 2,000 rain gauges. ARFs were calculated for a large number of circular sample catchments; storm durations of one, two and three days; areas up to $8000 km^2$; and recurrence intervals of 2, 5, 10, 20, 50 and 100 years. Although they found “small, but statistically significant, differences in ARF values for different parts of Victoria,” there was insufficient information to recognize patterns in the ARFs based on geographic location. An increasing tendency in the ARFs with the recurrence intervals was also found.

Similarly, [Asquith and Famiglietti \(2000\)](#) proposed an “annual maxima centered approach” for estimating ARFs. In their method, assuming an isotropic precipitation field, the annual maximum precipitation depth of each rain gauge station is first estimated, and then the concurrent precipitation observed at the neighbor gauges is used to determine the spatial structure of the storm. ARF values for one-day storms for Houston, Dallas and Austin, in Texas, were estimated, and the resulting values were found to be lower than those proposed in TP-29. For their dataset, [Asquith and Famiglietti \(2000\)](#) found dependency of the ARFs on geographic location and increasing values as the storm recurrence interval increased.

Alternative analytical approaches for converting point precipitation into areal precipitation have been presented by [Rodriguez-Iturbe and Mejia \(1974\)](#), [Sivapalan and Blöschl \(1998\)](#), and [De Michele et al. \(2001\)](#), among others. A frequent – and arguable – assumption in

their approaches is the representation of the precipitation field as isotropic; that is, the spatial correlation structure of the precipitation field depends only on distance and not on direction. Based on this fundamental assumption, [Rodriguez-Iturbe and Mejia \(1974\)](#) proposed a methodology in which the ARFs depend solely on the expected correlation coefficient between the precipitation depths at two randomly chosen points. [Sivapalan and Blöschl \(1998\)](#), likewise, proposed a method for constructing intensity-duration-frequency (IDF) curves, which consists of the areal averaging of the parent rainfall and the transformation of the parent rainfall distribution into an extreme value distribution. Similarly, after obtaining a scaling relation of average rainfall intensity in area and duration, [De Michele et al. \(2001\)](#) calculate ARFs of extreme rainfall events from their spatial and temporal scaling properties, based on dynamic scaling and statistical self-affinity.

With the advent of radar technology, spatially denser precipitation data have become available. In the United States, these data are called NEXRAD and are distributed by the United States National Weather Service with a resolution of approximately $4 \text{ km} \times 4 \text{ km}$ ([Fulton et al. 1998](#)). [Frederick et al. \(1977\)](#) state that since ARFs estimated from radar-based precipitation data are expressed as “dimensionless ratios of areal average precipitation to point precipitation, both being estimated from radar digits, [...] the uncertainties [in the] Z-R relationships are in part ‘divided out’.” They also mention that the estimation of ARFs for relatively large areas (i.e., greater than $1,000 \text{ km}^2$) based on gauge data alone has not been possible, and that this problem can be overcome with the use of radar data. In their study, [Frederick et al. \(1977\)](#) estimate ARFs of areas consisting of square precipitation cells. Likewise, [Bacchi and Ranzi \(1996\)](#) present a stochastic derivation of ARFs “based on the analysis of the crossing properties of the rainfall process aggregated in space and time.” They state that “radar data is more efficient than usual rain gauge networks in capturing the internal structure and the spatial distribution of storms,” and that for estimating ARFs “not actual intensity values, but the ratio between areal and point intensities, are needed.” They also indicate that “the use of radar data should give at least as reliable results as those achievable by using only gauge data, unless very dense and large [precipitation gauge] networks are available.” Similarly, [Omolayo \(1993\)](#) studied the applicability of the ARF values recommended in TP-29 for the United States in Australia and concluded that they are “probably satisfactory ... for estimating 24-hr area rainfalls for areal sizes between 200 and 500 km^2 .” [Omolayo \(1993\)](#) also mentions the inadequacy of point rainfall

for estimating areal rainfall of a particular frequency with the storm-centered approach. [Durrans et al. \(2002\)](#), in turn, evaluated ARFs for the Arkansas-Red River basin using the methodology of TP-29 and NEXRAD data of approximately 7 years. The precipitation grid of 159×335 cells that encompassed the Arkansas-Red River basin was sub-divided into 100 analysis areas each of which was represented by 16×33 cells. Their results are “consistent” with TP-29, although differences clearly exist. Because of the short period of record and the data heterogeneities (over time) caused by the continuous improvements in the algorithms, the authors consider their results preliminary. [Durrans et al. \(2002\)](#) also indicate that “because of the spatial coverages of rainfall fields that are provided by radar installations, radar-rainfall data appear uniquely suited to applications involving developments of depth-area relationships,” and that “few gauging networks are dense enough to provide the same degree of spatial detail.”

In this report, the estimation of ARFs in Texas using NEXRAD data is presented. Researchers calculated ARFs for different regions of Texas, storm durations, storm areas, precipitation depths, storm shapes and orientations, and seasons. Because the anisotropy of the storm field was an important matter of study, the storm-centered ARF calculation method was used. Likewise, because of the continuous improvements to the NEXRAD algorithms, which cause the data not to be homogeneous over time, only data for years 2003 and 2004 were considered in the study. This lack of long-term historical data prevented any type of frequency analysis and, instead, ARFs were related to rainfall depths for given durations (which correspond to specific return periods). On the other hand, the analysis was based on thousands of storm events, distributed over the 685,000-km² study area that took place in the 2-year period. The annual maximum storm-centered approach implemented in this study allowed us to study the anisotropic and seasonal characteristics of the storms.

2. PRECIPITATION DATA

Radar-based precipitation estimates are obtained by radar systems that emit electromagnetic waves of a given frequency and measure the reflectivity of the waves by the raindrops in the atmosphere. Each reflectivity value is then converted into precipitation rates using mathematical algorithms called reflectivity (Z) [in mm^6/m^3] – rain rate (R) [in mm/hr] relationships (i.e., Z-R relationships).

According to [Fulton et al. \(1998\)](#), in the United States, radar-based precipitation data are estimated as part of the NEXRAD federal program. The NEXRAD program is a tri-agency initiative of the National Weather Service (U.S. Department of Commerce), the Federal Aviation Administration (U.S. Department of Transportation) and the Air Force Air Weather Service and Naval Oceanography Command (U.S. Department of Defense). It has resulted in the delivery of over 160 S-band Weather Surveillance Radar-1988 Doppler (WSR-88D) radars across the country. The first radars were deployed in 1991 and the last ones in 1997. The NEXRAD program has been a major component of the ongoing technology modernization of the NWS and has revolutionized weather forecasting in the United States. In particular, it has greatly improved the NWS hydrologic forecasting and warning program. Through the River Forecasting Centers (RFC), the NWS distributes NEXRAD spatially distributed precipitation estimates in gridded format for the entire United States.

There are 12 WSR-88D radars in Texas plus several close to the state border, which cover well the study area with the exception of the Big Bend zone in southwest Texas (Figures [2.1](#) and [2.2](#)).

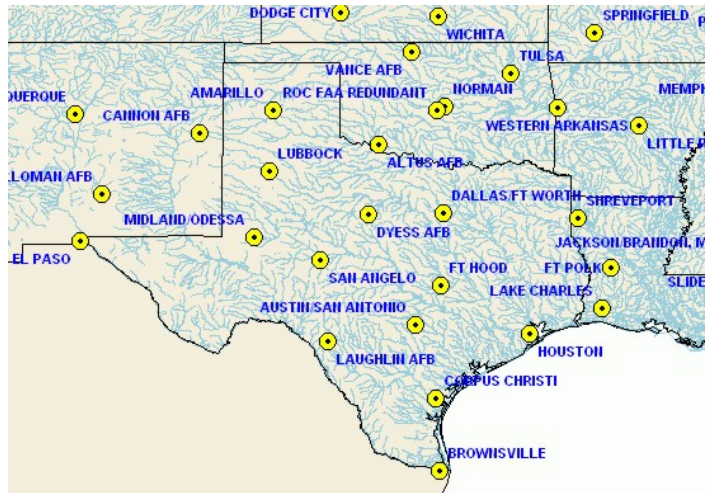


Figure 2.1: Texas WSR-88D Radars (Source: U.S. National Weather Service, <http://www.roc.noaa.gov/interactive/defaultIE.asp>).

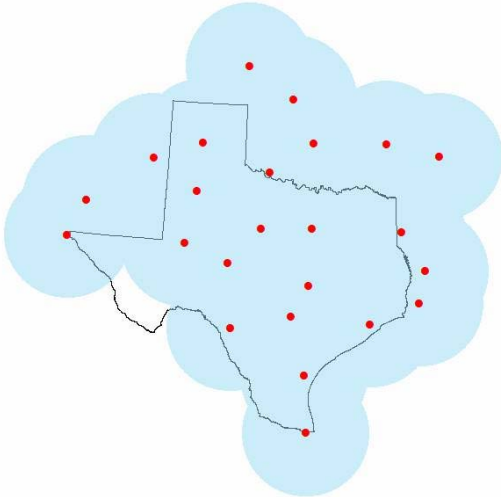


Figure 2.2: Scanning Domain of the Radars within and around Texas. Red Points: Radar Locations; Blue Area: Radar Scanning Domain; and Black Outline: Texas Border.

To estimate precipitation rates, reflectivity is measured in every cell of a radar’s polar grid, which corresponds to the area covered by a radar (i.e., the area within a distance of approximately 230 km from the radar). In this polar grid, each grid cell has a radial length of 1 km and an azimuthal angle of 1°, giving more than 80,000 cells with an average area of approximately 2 km². Once reflectivity in each cell is known, the values are converted into rain rate using Z-R relationships. According to the NWS (2002), initially, only the $Z = 300 R^{1.4}$ relationship was used, which applied to convective storms. Though it worked well for deep

convective precipitation systems, it underestimated, often severely, other types of storms. In 1997, the $Z = 250 R^{1.2}$ relationship was proposed, which applied to hurricanes, tropical storms and small scale deep-saturated storms fed by tropical oceanic moisture. Likewise, in 1999, the $Z = 200 R^{1.6}$ relationship was developed for general stratiform events, and $Z = 130 R^{2.0}$ and $Z = 75 R^{2.0}$ for winter stratiform events east and west of the continental divide, respectively. After estimating the rain rate in every cell, the values obtained for each two consecutive radial cells are averaged defining a new polar grid in which the cells have a radial length of 2 km and the same azimuthal angle of 1° . Further corrections are then applied to account for the existence of hail cores in the thunderstorm clouds, which produce extremely high reflectivities that can be misinterpreted as unusually high rain rates; abnormal rain rate changes over time in a cell; or signal degradation from partial beam filling, which may reduce the estimates at far ranges (Fulton et al. 1998). The hourly digital precipitation array (DPA) is then remapped from the polar array in which the rain rates are computed onto the Hydrologic Rainfall Analysis Project (HRAP) grid, which is a grid that covers the conterminous United States. The HRAP grid cell size ranges from about 3.7 km at southern U.S. latitudes to about 4.4 km at northern U.S. latitudes. A square HRAP grid of 131×131 cells, centered at the radar, covers the 230-km range domain of the WSR-88D rainfall estimates. The DPA is mapped to this common grid so that it can be mosaicked with other DPAs across the country in subsequent regional and national rainfall processing. The resulting hourly precipitation estimates constitute the *Stage I* NEXRAD data.

Stage II NEXRAD data provide an optimal estimate of hourly rainfall using a multivariate objective analysis scheme incorporating both radar and rain gauge observations. This multisensor estimate of rainfall is performed once per hour for each radar on the HRAP grid using as input the hourly DPA product from Stage I and all available rain gauge data (Fulton et al. 1998). First, a uniform mean field gauge–radar bias is applied using a Kalman filter approach. This adjustment, in the form of a gauge–radar multiplicative bias, is applied uniformly over each WSR-88D scanning domain and, therefore, is called *mean field bias* adjustment. Because these computed hourly biases are representative of the total scanning domain, they do not account for the spatial variability of the bias within individual storms. Thus, the mean field bias adjustment is expected to account for spatially uniform radar estimation errors such as hardware miscalibration, wet radome attenuation and inappropriate Z – R coefficients. Next, a second

nonuniform bias is applied, which may vary depending on the range, azimuthal angle, rainfall type and other factors. To account for the spatial heterogeneity, the rainfall estimates are locally adjusted using a multivariate optimal estimation procedure that incorporates observed gauge data. In this estimation procedure, the weights for radar and gauge estimates at each HRAP grid cell are determined such that their linear combination minimizes the expected error variance of the estimate. A decreasing (increasing) weight is placed on the gauge (radar) accumulation as the distance increases away from the gauge. Likewise, Stage III NEXRAD data are obtained by mosaicking Stage II rainfall estimates from radars with overlapping scanning domains. Finally, Multisensor Precipitation Estimator (MPE) NEXRAD data take advantage of precipitation values from satellites in addition to those from radars and rain gauges. Satellite data are of great importance for filling up the areas that are not covered by radars or rain gauges, such as the Big Bend area in southwest Texas. With respect to Stage III, MPE also improves the mosaicking and local bias correction algorithms (Seo 2003). A discussion on the algorithms for adjusting precipitation estimates to gauge data is presented by Young et al. (2000).

Unavoidably, in the long process that expands from measuring reflectivity to estimating precipitation depths, different errors can be made (NWS 2002). The vertical profile reflectivity (VPR) effect, for example, can induce overestimation of reflectivity by a factor of 2 and underestimation by a factor of 10. The erroneous reflectivity is obtained when the radar detector samples the electromagnetic waves that hit the raindrops in the freezing level, which is located as low as 2 km above the ground level in the cold season. The VPR effect is more pronounced in the areas that are far from the radar. Likewise, the selection of the appropriate Z-R relationship for the specific rainfall characteristics (i.e., tropical, stratiform or convective) affects the precipitation estimates. Inconsistent sampling of electromagnetic waves (i.e., number of pulses per sampling volume, number of scans per hour, beam width, among others) can also affect the resulting estimates, but it is usually limited to geographically small locations. Finally, even though the mean field bias adjustment enhances the overall quality of the radar measurement, it can induce errors at specific locations.

Radar-based precipitation data have been widely used in different hydrologic applications including rainfall runoff modeling and real-time flood warning systems (Ogden and Julien 1994; Bedient et al. 2000; Ogden et al. 2000; Smith et al. 2001; Giannoni et al. 2003; Bedient et al. 2003; Vieux and Bedient 2004; Vieux and Vieux 2004; Moon et al. 2004). Notwithstanding the

fact that NEXRAD precipitation data are subject to inaccuracies due to a variety of error sources (NWS 2002), at present, it is the only continuous spatially distributed precipitation database available countrywide at its resolution.

According to Durrans et al. (2002), “the most significant limitations of radar-rainfall data, both for frequency analysis and for development of depth-area relationships, are the shortness of the records and the heterogeneities caused by continual improvements to the data processing algorithms.” Because of this shortness of the records and data heterogeneities, only data for years 2003 and 2004 were considered in the study. This lack of long-term historical data prevented any type of frequency analysis and, instead, ARFs were related to rainfall depths for given durations (which correspond to specific return periods). On the other hand, the analysis was based on more than 17,500 storm events of different durations that took place in the 2-year period, distributed over the 685,000-km² study area. This project used both MPE and Stage III NEXRAD data for comparison purposes. Since Texas falls completely within the West Gulf River Forecasting Center (WGRFC) area, the data were obtained for that specific RFC from the NWS website (NWS 2005). The area served by the WGRFC comprises the drainage area of the Texas Gulf including the Sabine River and the Rio Grande. The hourly DPA is distributed in HRAP grid format and covers a much larger area than that served by the WGRFC (Figure 2.3).

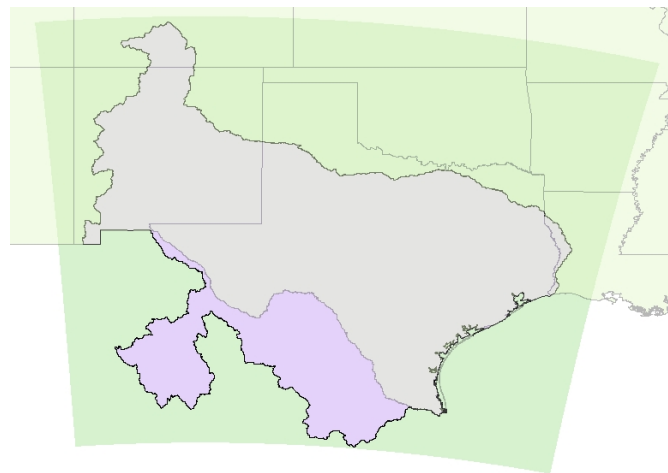


Figure 2.3: Area Served by the West Gulf River Forecasting Center (Purple) and HRAP Grid Extent in Which the Data Are Distributed (Green).

3. METHODOLOGY

Stage III and MPE hourly precipitation estimates for the years 2003 and 2004 were obtained for the WGRFC HRAP grid (Figure 3.1). The WGRFC HRAP grid has 165,750 cells (390 rows \times 425 columns) and covers an area significantly larger than the state of Texas.

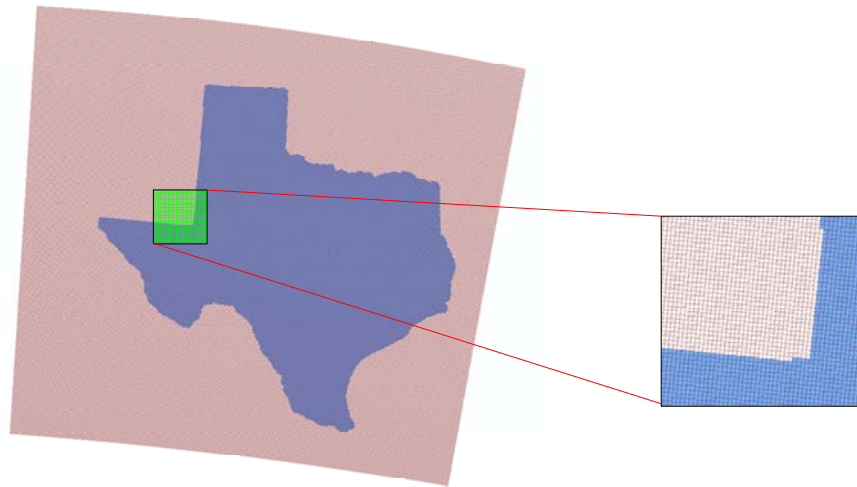


Figure 3.1: West Gulf River Forecasting Center HRAP Grid.

Therefore, to limit the calculations to the study area, the grid was clipped out by a polygon that buffered Texas around by 50 km, resulting in only 56,420 cells (Figure 3.2).



Figure 3.2: 50-km Buffer around Texas.

For each cell of the clipped grid, the annual maximum precipitation depth was calculated, and its value was stored along with its corresponding time of occurrence. For durations other than 1 hr (which is the time step of the original dataset), a moving window over time was defined so that the annual maximum accounted for the consecutive hours that generated the maximum depth for the given duration. As a result, grids of annual maxima and date of occurrence for durations of 1 hr, 3 hrs, 6 hrs, 12 hrs and 24 hrs were generated.

ARF calculations were conducted only for those cells in which: (1) the annual maximum was greater than a threshold depth value; and (2) the cell value was the greatest in a 21×21 -cell square window, centered at the cell, of concurrent precipitation. The threshold values were 20 mm for a storm duration of 1 hr, 25 mm for 3 hrs, 30 mm for 6 hrs, 30 mm for 12 hrs and 40 mm for 24 hrs, and correspond approximately to the 2-year precipitation depth for the given duration according to TP-40 (U.S. Weather Bureau 1961). The requirement that the cell has to have the greatest value in the neighborhood is necessary to ensure that the cell is the storm center (Figure 3.3).

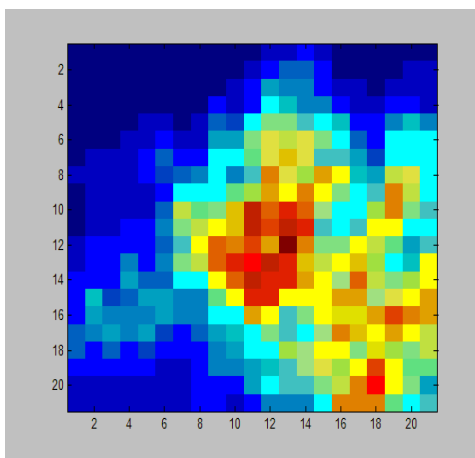


Figure 3.3: 1-hr Duration Concurrent Precipitation Field for June 4, 2003, at 6:00 am. The Color of Each Cell Represents the Precipitation Depth. Red Cells Have Higher Precipitation Depth than the Blue Ones.

After selecting the cells that satisfy the conditions, ARFs were calculated for these cells only. Table 3.1 indicates the number of cells for which ARFs were calculated per storm duration, year and type of NEXRAD data, and Figure 3.4 shows their location for the specific case of a 1-hr duration, year 2003 and Stage III data. In Figure 3.4, note that the cells are well distributed

over the entire study area with the exception of the Big Bend area for which Stage III data are not available because it is outside the radars' scanning domain.

Table 3.1: Number of Cells for Which ARFs Were Calculated.

| Duration (hrs) | Stage III | | MPE | |
|-------------------|-----------|------|------|------|
| | 2003 | 2004 | 2003 | 2004 |
| 1 | 6900 | 7505 | 5314 | 7553 |
| 3 | 3287 | 3720 | 3212 | 3961 |
| 6 | 3096 | 2633 | 2290 | 2664 |
| 12 | 1827 | 1999 | 1745 | 2047 |
| 24 | 1675 | 1617 | 1474 | 1621 |

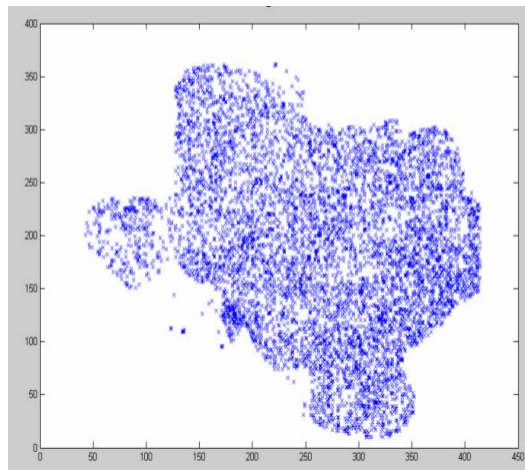


Figure 3.4: Location of the Cells for Which ARFs Were Calculated for a Storm Duration of 1 hr and Using Stage III Data of 2003.

For a given selected cell, ARFs are then calculated using concurrent precipitation estimates for elliptical storms. The ellipse that describes the shape of the storm is centered at the cell and is defined such that, for a given area, it maximizes the precipitation volume within it. In the following, this ellipse that maximizes the volume is called the “optimum ellipse.” The ARFs are calculated according to

$$ARF_{A_0} = \frac{\frac{1}{A} \iint_{A_0} P \, dA}{P_0} \quad (3.1)$$

where $\iint_{A_0} P \, dA$ [L^3] is the precipitation volume in the optimum ellipse A_0 , A [L^2] is the area of the optimum ellipse A_0 , P_0 is the precipitation at the cell, and ARF_{A_0} is the areal reduction factor for the cell and area A . Note that there can be several optimum ellipses of different areas centered at the same cell, thus giving different ARFs for different areas. Note, as well, that all concurrent precipitation values can be retrieved because the time of occurrence of the cell maximum was previously stored.

To determine the optimum ellipse, for a given cell and area, its aspect (i.e., the ratio of its longer diameter to its shorter diameter) and orientation (i.e., angle formed by its longest diameter and the west-east axis) are changed systematically using a heuristic approach until the volume inside the ellipse is maximized. For computational efficiency, however, the aspect was bound to values equal to or lower than 5. The procedure was repeated for all the selected cells, storm durations of 1, 3, 6, 12 and 24 hrs, and areas equivalent to those of 3, 5, 7, 9, 11, 19, 37 and 49 cells. These areas correspond approximately to 48, 80, 112, 144, 176, 304, 592 and 784 km^2 , but are not exactly those values because the cell areas are not all the same (Figure 3.5). The procedure was conducted for both Stage III and MPE data, and for years 2003 and 2004.

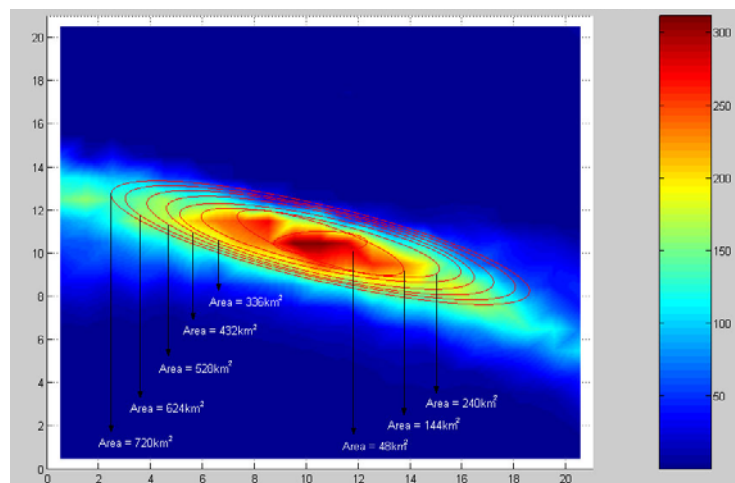


Figure 3.5: Ellipses of Different Areas Shown on a Precipitation Field. Each Ellipse Has Its Own Aspect and Inclination Angle.

After the ARFs are calculated, they are plotted in ARF vs. area graphs to estimate their change rate as the area increases. In addition to the dependency of ARFs on the storm duration, their dependency on rainfall depth and geographic region has been studied.

4. RESULTS AND ANALYSIS

The result of the ARF calculation was a 255,048-row and 10-column table, in which each row corresponded to an ARF calculation and the columns were X-coordinate, Y-coordinate, storm duration, precipitation depth in the cell, time of occurrence in the year, ellipse area, ellipse aspect, ellipse orientation, geographic region and areal reduction factor. In the following, and for the sake of brevity, these variables are referred to as X, Y, duration (t_d), depth (D), hour (H), area (A), aspect (ρ), orientation (θ), region and areal reduction factor (ARF). These data were analyzed to find patterns and relationships between the different variables. As mentioned above, previous studies show that ARFs decrease with area and increase with duration; however, noteworthy variability was found also with region and depth (Figures 4.1 and 4.2).

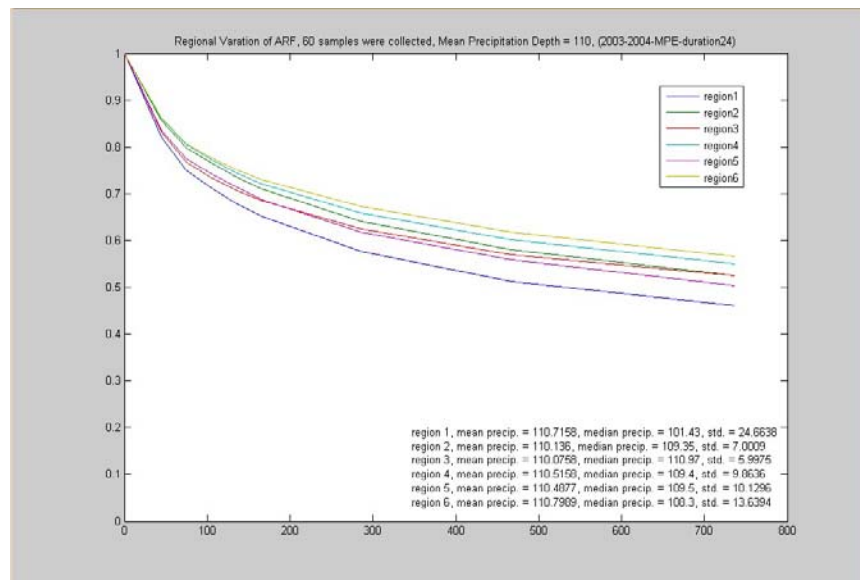


Figure 4.1: Effect of Location on the ARF Values.

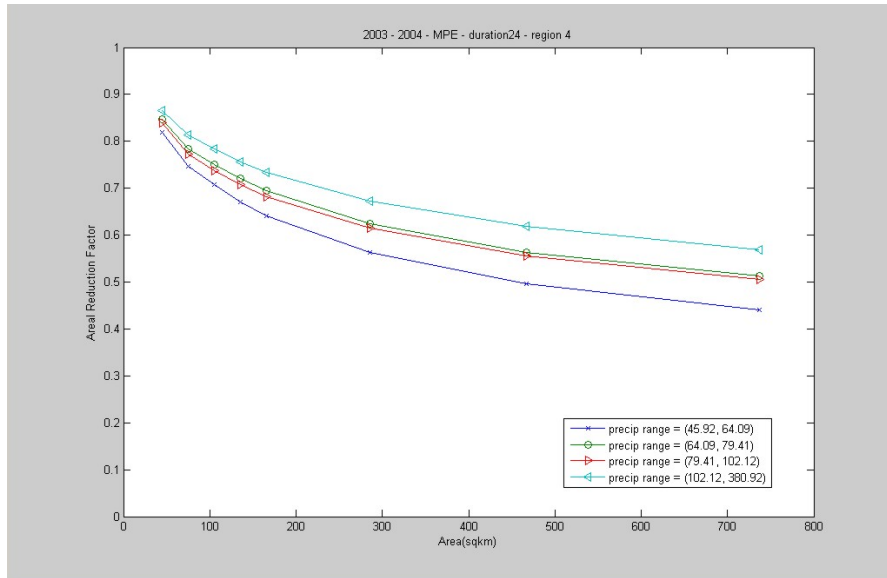


Figure 4.2: Effect of Precipitation Depth on the ARF Values.

The six regions referred to in the figures were defined based on climatological conditions and are the same subdivision used in previous hydrologic studies supported by the Texas Department of Transportation (TxDOT) (Carr 1967; USGS 1998) (Figure 4.3).

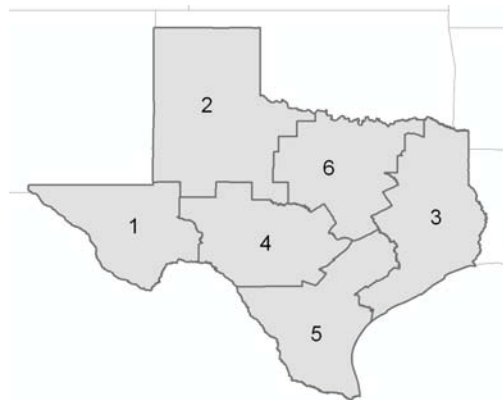


Figure 4.3: Regions of Texas (U.S. Geological Survey 1998).

In Figure 4.1, there is an ARF-area curve for each region, and each of them was based on 60 storms (i.e., a total of 360 storms) with average depth of around 110 mm. Having set all other variables equal, the region is left as the explaining variable for the differences. Likewise, in Figure 4.2, there is an ARF-area curve for each depth range, and each was based on all storms that took place in Region 4. In this case, having set all other variables equal, the depth is left as

the explaining variable for the differences. Other variables, such as aspect and orientation of the ellipse and hour, did not show a significant effect on the value of the ARFs, but they were also studied.

ARF-AREA EQUATIONS

The dataset was subdivided into 240 subdatasets, each of them containing the records that had the same duration (i.e., five different values), area (i.e., eight different values) and region (i.e., six different regions). Typically, each subset had more than 1,000 records. The values from the subsets that corresponded to the same region and duration were then plotted in ARF-area charts. There were a total of 30 charts, each of them with a subset of points for each of the eight different areas (Figure 4.4).

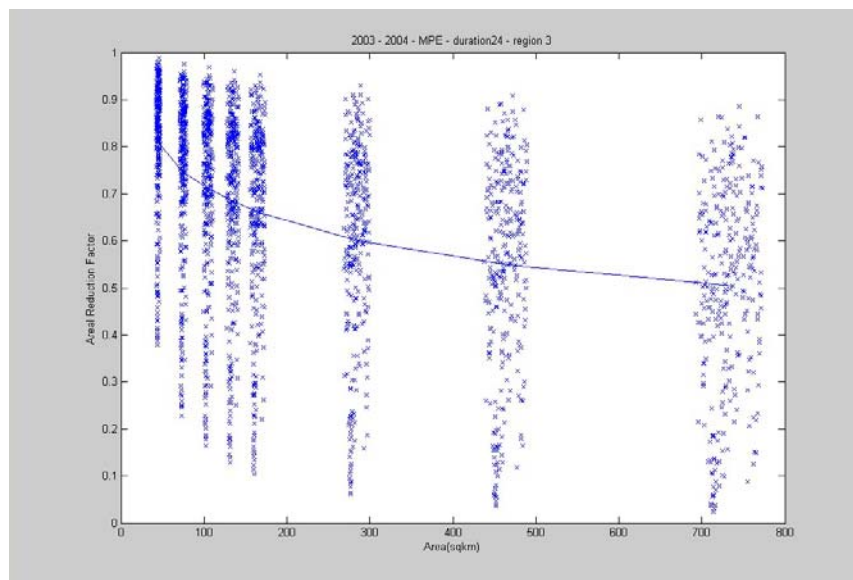


Figure 4.4: ARF-Area Plot for Region 4 and Storm Duration of 24. Note the Scatter of the Points around the Mean Line, Which Is Presumed to Be Caused by the Differences in Precipitation Depth.

The horizontal scatter of each subset is caused by the fact that the area values are the same when measured in number of cells, but vary somewhat when measured in square kilometers. To explain the variability of the ARF values, the subsets were further subdivided into four groups based on the depth quartiles. Analysis of variance (ANOVA) tests and Tukey's W

procedure (Ott and Longnecker 2001) were conducted to verify that – for a given region, duration and area – the means of the ARF values for the different depths were statistically different. ANOVA tests are used to examine if there is a statistical difference among various population means. In the ANOVA test, the null hypothesis states that the means of all populations are not statistically different. In this study, accepting the null hypothesis with a significance level of 0.05 implied that the ARF values are not affected by the precipitation depth. On the other hand, rejecting the null hypothesis with a significance level of 0.05 implied that at least one of the population means was different from the others. In such a case, the Turkey’s W procedure was then applied to single out the populations whose means were different. In most cases, the ARF values for different depths proved to be statistically different with a significance level of 0.05, but the depth effect was neglected when the level of significance dropped below 0.05.

Regression equations were determined for the means of each depth group of each of the 30 charts. It was found that the ARFs showed a decay tendency with the increase of area according to

$$ARF = 1 - c A \quad (4.1)$$

for areas less than 45 km² and

$$ARF = a \log (A) + b \quad (4.2)$$

for areas greater than 45 km², where a, b and c are constants that vary with region, duration and depth, and the area is in km². The values of a, b and c are given in Tables 4.1 to 4.5 for the different durations and regions. Whenever it was found that they were not statistically different, the regression curves were collapsed. That explains why there are less than four sets of constants for each combination of region and duration. It was also observed that the regression equations were clearly different for the different regions. Finally, according to the depth-duration-frequency curve concept, depth and frequency are related for a given duration. So, since it was observed that the ARFs increased with depth, it was concluded that they also increase with return period.

Table 4.1: Values of a, b and c for a Duration of 1 hr.

| | Depth Range | a | b | c |
|-----------------|--------------------|----------|----------|----------|
| Region 1 | all depths | -0.175 | 1.49 | 0.00385 |
| Region 2 | all depths | -0.178 | 1.52 | 0.00353 |
| Region 3 | all depths | -0.164 | 1.45 | 0.00383 |
| Region 4 | d < 38 mm | -0.174 | 1.46 | 0.00448 |
| | d > 38 mm | -0.167 | 1.46 | 0.00397 |
| Region 5 | d < 36 mm | -0.170 | 1.44 | 0.00446 |
| | d > 36 mm | -0.168 | 1.47 | 0.00366 |
| Region 6 | all depths | -0.161 | 1.46 | 0.00341 |

Table 4.2: Values of a, b and c for a Duration of 3 hrs.

| | Depth Range | a | b | c |
|-----------------|--------------------|----------|----------|----------|
| Region 1 | all depths | -0.160 | 1.44 | 0.00376 |
| Region 2 | all depths | -0.152 | 1.44 | 0.00303 |
| Region 3 | all depths | -0.143 | 1.39 | 0.00339 |
| Region 4 | d < 46 mm | -0.157 | 1.42 | 0.00393 |
| | 46 mm < d < 74 mm | -0.146 | 1.39 | 0.00363 |
| | d > 74 mm | -0.146 | 1.43 | 0.00269 |
| Region 5 | d < 66 mm | -0.157 | 1.42 | 0.00387 |
| | d > 66 mm | -0.151 | 1.45 | 0.00268 |
| Region 6 | d < 56 mm | -0.132 | 1.34 | 0.00353 |
| | d > 56 mm | -0.135 | 1.41 | 0.00244 |

Table 4.3: Values of a, b and c for a Duration of 6 hrs.

| | Depth Range | a | b | c |
|-----------------|--------------------|----------|----------|----------|
| Region 1 | d < 76 mm | -0.154 | 1.41 | 0.00398 |
| | d > 76 mm | -0.143 | 1.42 | 0.00267 |
| Region 2 | all depths | -0.144 | 1.42 | 0.00281 |
| Region 3 | all depths | -0.134 | 1.36 | 0.00329 |
| Region 4 | d < 52 mm | -0.145 | 1.38 | 0.00388 |
| | 52 mm < d < 84 mm | -0.145 | 1.40 | 0.00329 |
| | d > 84 mm | -0.133 | 1.39 | 0.00269 |
| Region 5 | d < 102 mm | -0.146 | 1.40 | 0.00338 |
| | d > 102 mm | -0.128 | 1.39 | 0.00210 |
| Region 6 | d < 52 mm | -0.144 | 1.37 | 0.00398 |
| | d > 52 mm | -0.124 | 1.37 | 0.00230 |

Table 4.4: Values of a, b and c for a Duration of 12 hrs.

| | Depth Range | a | b | c |
|-----------------|--------------------|----------|----------|----------|
| Region 1 | all depths | -0.147 | 1.41 | 0.00341 |
| Region 2 | all depths | -0.138 | 1.34 | 0.00277 |
| Region 3 | d < 66 mm | -0.145 | 1.36 | 0.00436 |
| | d > 66 mm | -0.113 | 1.30 | 0.00280 |
| Region 4 | d > 72 mm | -0.140 | 1.38 | 0.00344 |
| | d < 72 mm | -0.124 | 1.34 | 0.00299 |
| Region 5 | d < 111 mm | -0.144 | 1.41 | 0.00314 |
| | d > 111 mm | -0.125 | 1.38 | 0.00216 |
| Region 6 | d < 61 mm | -0.121 | 1.29 | 0.00385 |
| | d > 61 mm | -0.121 | 1.37 | 0.00207 |

Table 4.5: Values of a, b and c for a Duration of 24 hrs.

| | Depth Range | a | b | c |
|-----------------|--------------------|----------|----------|----------|
| Region 1 | all depths | -0.140 | 1.38 | 0.00346 |
| Region 2 | all depths | -0.127 | 1.37 | 0.00250 |
| Region 3 | all depths | -0.114 | 1.297 | 0.00311 |
| Region 4 | d < 64 mm | -0.142 | 1.40 | 0.00331 |
| | 64mm < d < 102mm | -0.129 | 1.34 | 0.00333 |
| | d > 102 mm | -0.112 | 1.32 | 0.00227 |
| Region 5 | d < 126 mm | -0.137 | 1.39 | 0.00305 |
| | d > 126 mm | -0.124 | 1.38 | 0.00201 |
| Region 6 | d < 67 mm | -0.141 | 1.36 | 0.00382 |
| | d > 67 mm | -0.108 | 1.31 | 0.00227 |

Figure 4.5 shows the resulting ARF-area curves for region 4 and duration of 24 hrs, and Figure 4.6 presents the ARF-area curve for region 4, duration of 24 hrs and depth between 64 mm and 102 mm along with the points used for obtaining the curve.

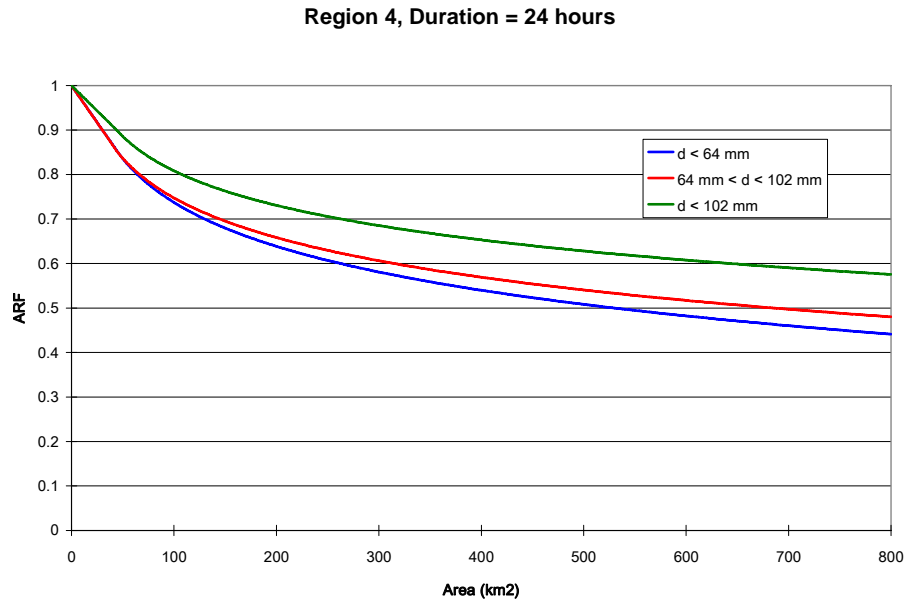


Figure 4.5: ARF-Area Plot for Region 4 and Duration of 24 hrs.

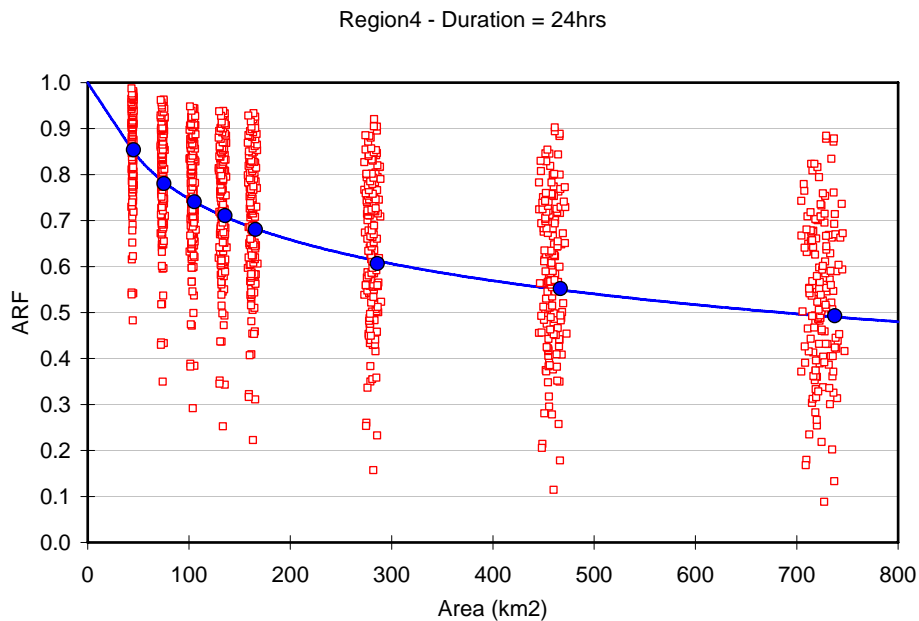


Figure 4.6: ARF-Area Plot for Region 4, Duration of 24 hrs and Depth between 64 mm and 102 mm.

ASPECT AND ANGLE OF OPTIMUM ELLIPSE

As mentioned above, aspect and orientation of the optimum ellipse did not have a large effect on the value of the ARFs. However, from the data available, it was possible to determine the predominant shape and orientation of the storms analyzed, and their regional distribution.

Normalized histograms of aspect for the different regions and durations are included in [Figure 4.7](#). It can be noticed that around one-third of the ellipses fell into the bins that represent aspect values between 1 and 2, which corresponds to almost-circular shapes. The remaining two-thirds of the storms had a clear elliptical shape with an aspect greater than 2. It was also observed that the frequency decreased as the aspect increase, but then increased again for the bin of 4.5 to 5. This abnormal increase was caused by the setting of the maximum value of the aspect to 5. Overall the same patterns were observed for the different regions and durations.

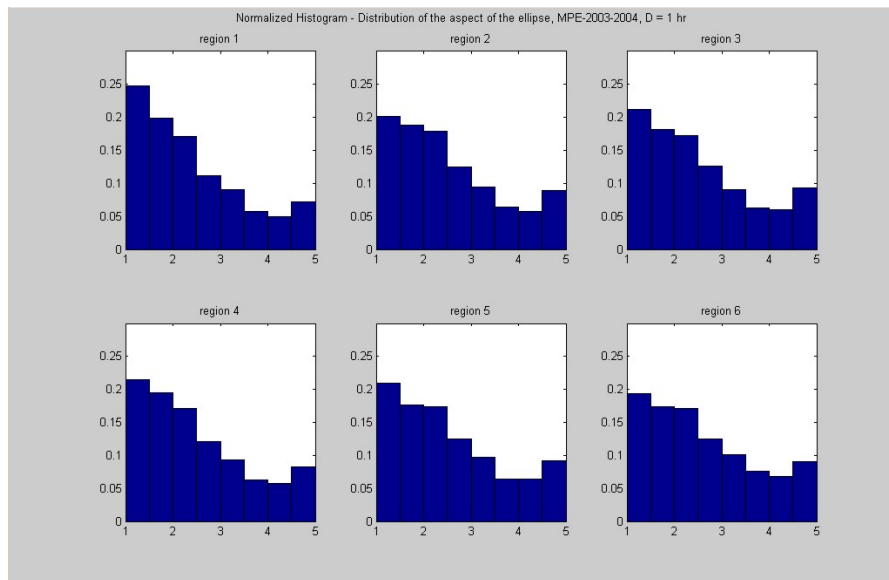


Figure 4.7a: Normalized Histograms of Aspect for a Duration of 1 hr.

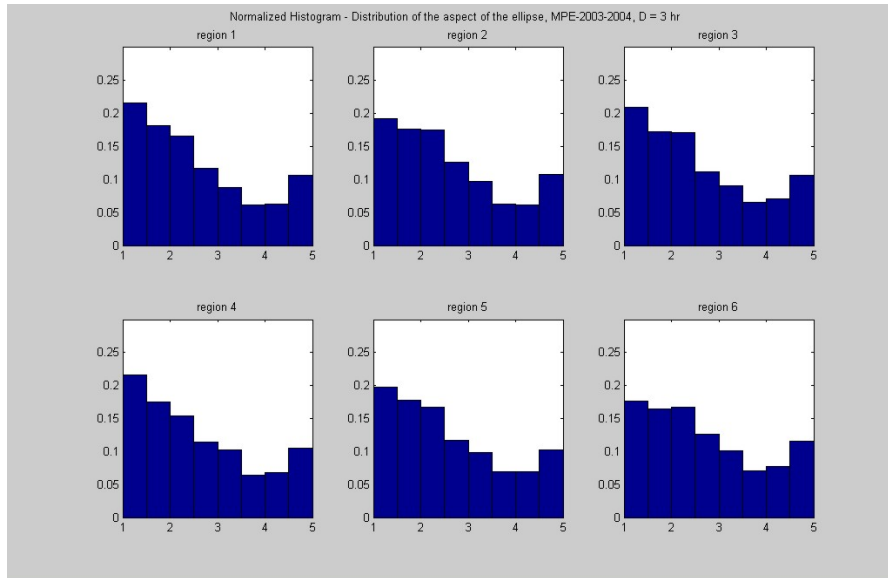


Figure 4.7b: Normalized Histograms of Aspect for a Duration of 3 hrs.

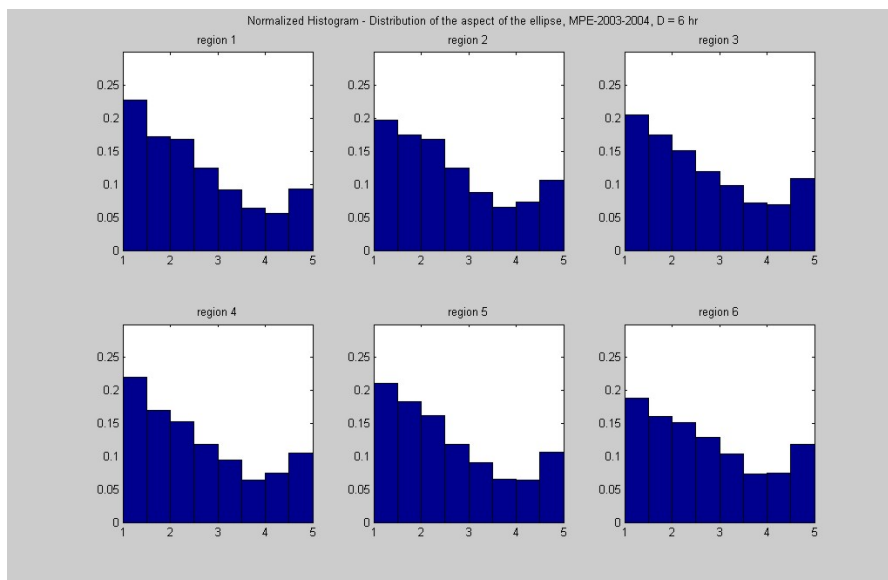


Figure 4.7c: Normalized Histograms of Aspect for a Duration of 6 hrs.

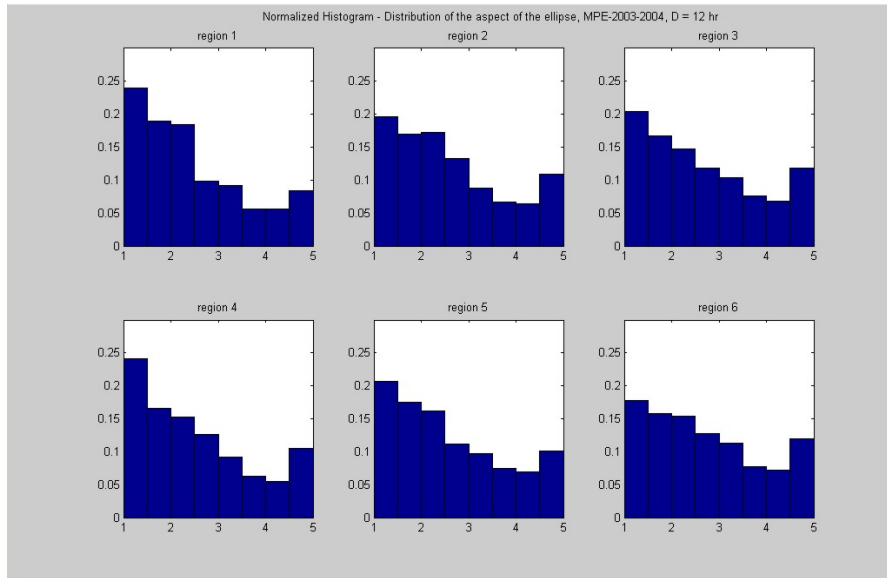


Figure 4.7d: Normalized Histograms of Aspect for a Duration of 12 hrs.

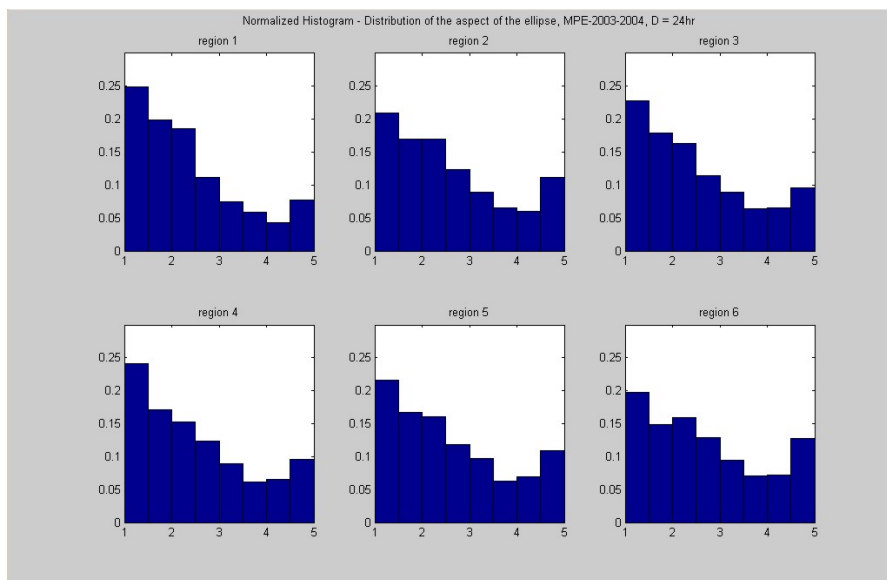


Figure 4.7e: Normalized Histograms of Aspect for a Duration of 24 hrs.

Similarly, normalized histograms of the orientation angle are presented in [Figure 4.8](#) for those ellipses with an aspect greater than 2. The aspect threshold of 2 was used because the angle was considered a trivial variable for almost-circular ellipses. In these histograms, an angle of 0° referred to an ellipse whose longer axis was parallel to the west-east direction, an angle of 45° to an ellipse whose longer axis was parallel to the southwest-northeast direction, and so on. In the histograms, regional variability is significant. Overall, a clear predominance of a 45° angle was

found for regions 3, 5 and 6, which was stronger for the shorter durations than for the longer durations (specially for region 6). Note that regions 3 and 5 are the two coastal ones. Likewise, for region 2, the predominant orientation angles were 0° and 45° ; for region 4, they were 0° , 45° and 90° , with slight preference for 90° ; and for region 1, also 0° , 45° and 90° , but with preference for 0° . Note that for all regions and durations, the angle of 135° had the lowest frequency and was around 10% to 15%.

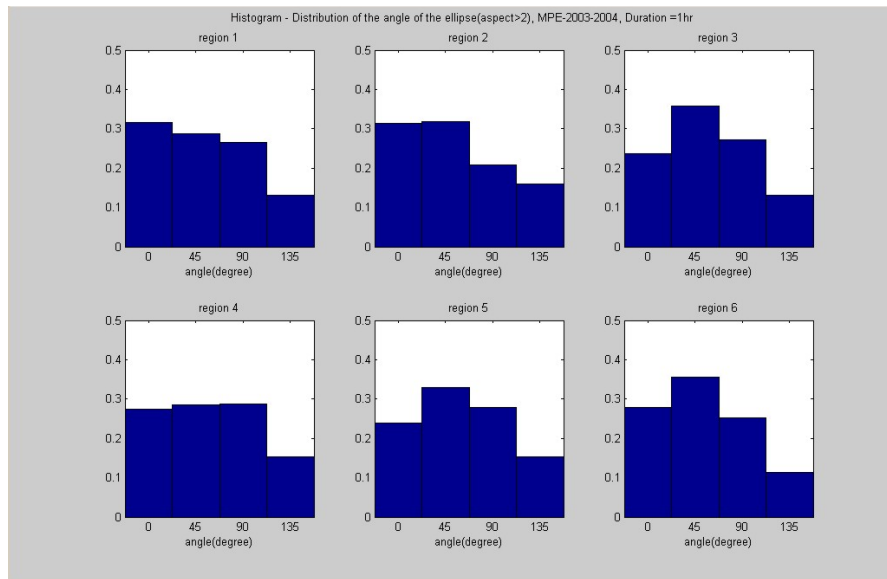


Figure 4.8a: Normalized Histograms of Angle for a Duration of 1 hr.

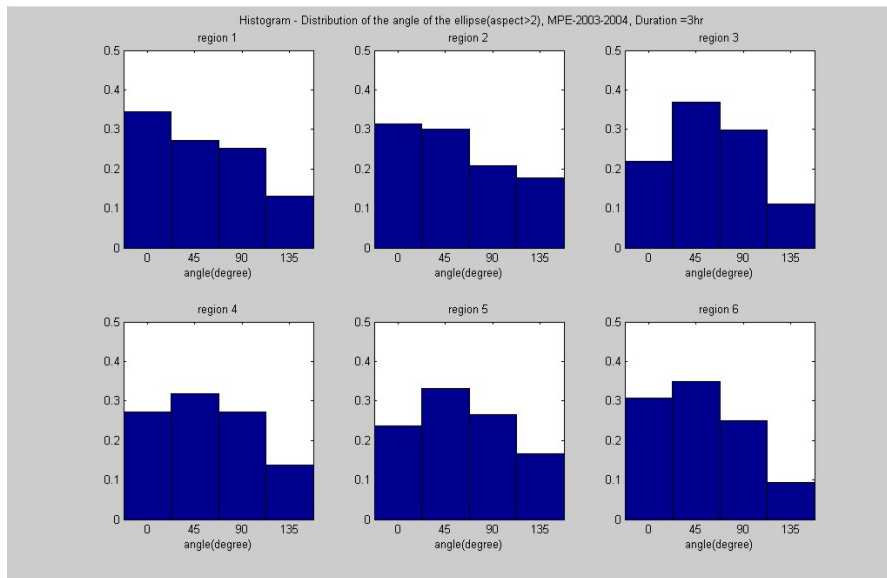


Figure 4.8b: Normalized Histograms of Angle for a Duration of 3 hrs.

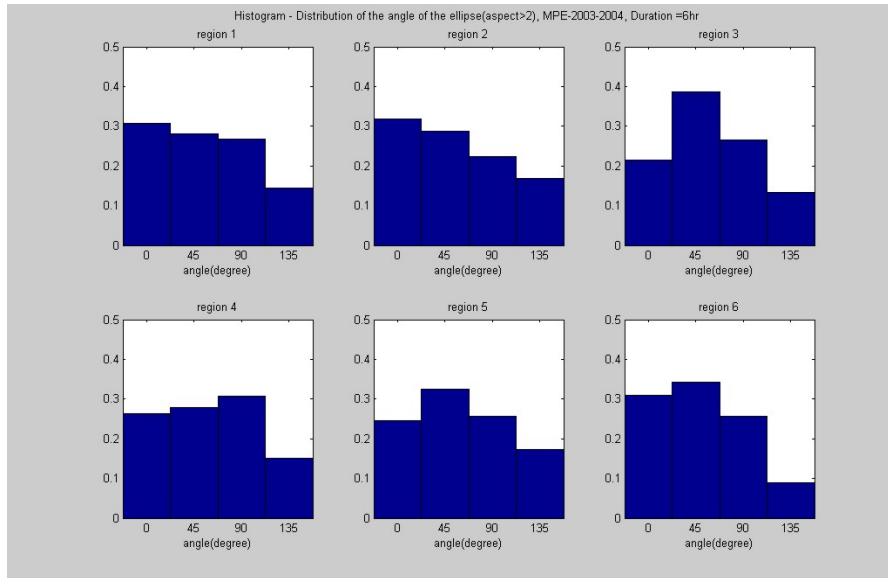


Figure 4.8c: Normalized Histograms of Angle for a Duration of 6 hrs.

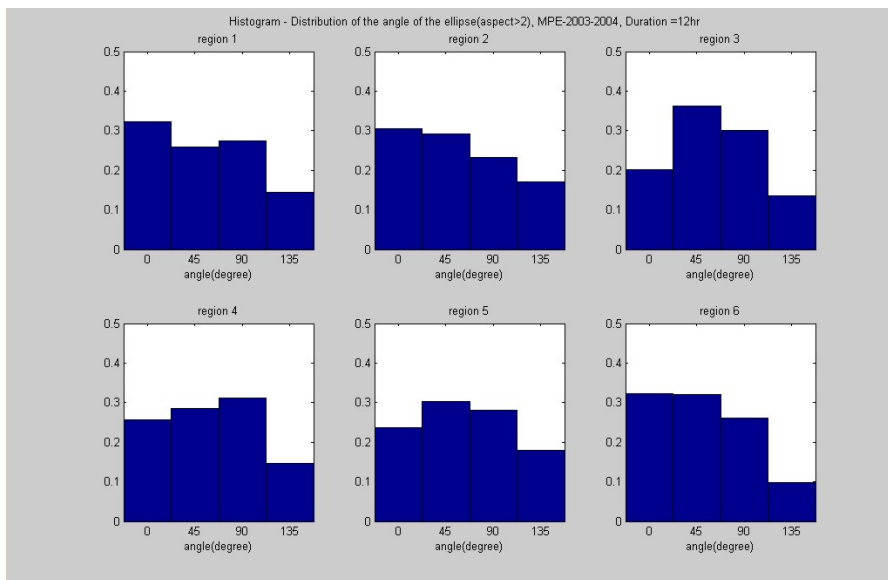


Figure 4.8d: Normalized Histograms of Angle for a Duration of 12 hrs.

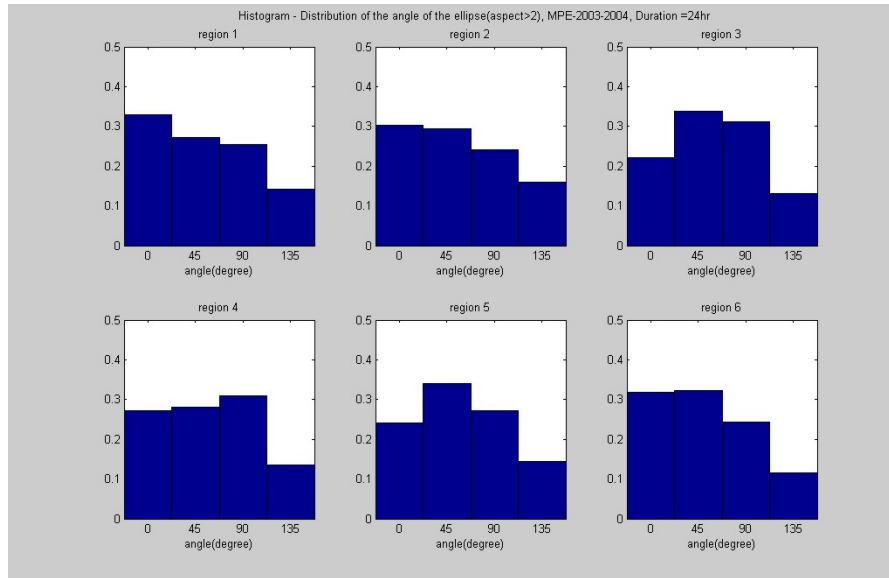


Figure 4.8e: Normalized Histograms of Angle for a Duration of 24 hrs.

These aspect and angle histograms confirm the need for accounting for anisotropy when analyzing storms.

COMPARISON WITH FORMER STUDIES

In general, lower ARF values were observed compared to previous studies ([U.S. Weather Bureau 1957](#); [Asquith and Famiglietti 2000](#); [Natural Environment Research Council 1975](#)). However, it should be noted that the TP-29 curves do not show any decreasing tendency after a certain threshold area. Considering the fact that the spatial extent of a storm is limited, it is reasonable to conclude that ARFs should decrease with the increase of area. Possible explanations of the differences between the ARF values calculated here and in previous studies include: (1) our values relate concurrent area to point precipitation, rather than annual mean values as TP-29 does; (2) precipitation ratios have a significant scatter as shown by [Asquith and Famiglietti \(2000\)](#); (3) our values account for the anisotropy of the precipitation field; and (4) our values were based on a 2-year set of spatially distributed radar-based precipitation estimates, rather than long records of point precipitation values. [Figure 4.9](#) shows the results of different studies for comparison purposes for region 4, duration of 24 hrs and depth between 64 mm and 102 mm.

Region 4 - Duration 24 hrs - Depth [64 mm, 102 mm]

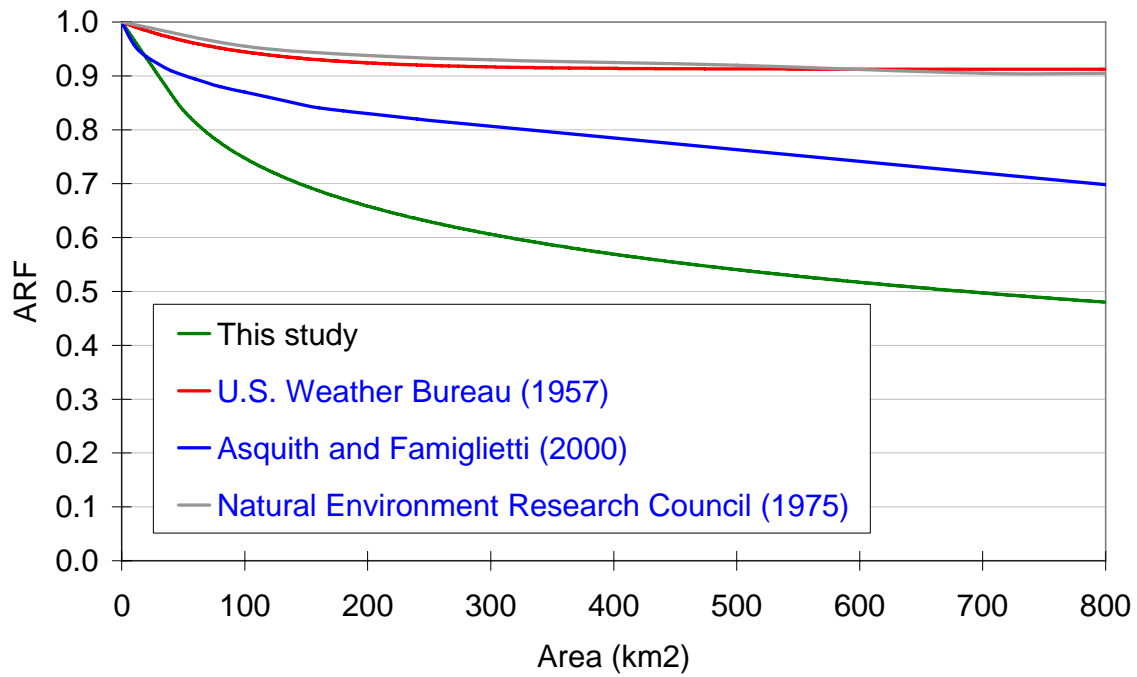


Figure 4.9: Comparison of ARF-Area Curves According to Different Studies.

5. ARCGIS_STORM DOCUMENTATION

ArcGIS_Storm is a graphical user interface program developed at Texas A&M University with the support of the Texas Department of Transportation. It develops hypothetical storms of different shapes and sizes based on user input. ArcGIS_Storm has been written and compiled in Visual Basic 6.0 and implemented in the Environmental Systems Research Institute's (ESRI) ArcGIS ArcMap as a customized toolbar (Figure 5.1).



Figure 5.1: ArcGIS_Storm Toolbar.

PROJECT SETUP

Click on the **Project Setup/Project working directory** menu (Figure 5.2) and the **Project Set Up** window will pop up (Figure 5.3). The project working directory is a container that will store all the outputs including geodatabases, shapefiles, text files and tables.

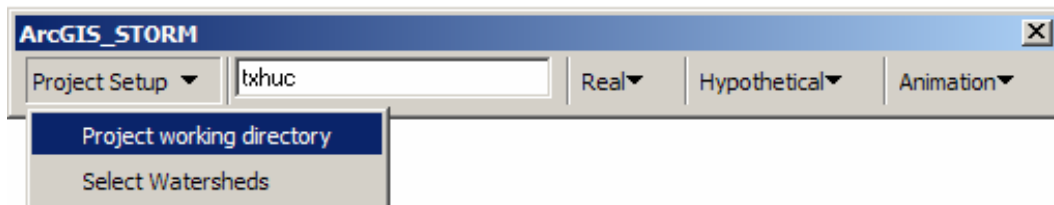



Figure 5.2: Project Working Directory Menu.

In the **Project Set Up** window (Figure 5.3), the user begins by selecting a working directory in the **Browsing Directory** frame. If you want to create a new directory, in the **Working Directory** frame, click on  and the **New Folder Name** window will pop up (Figure 5.4). In it, specify the name of your project folder.

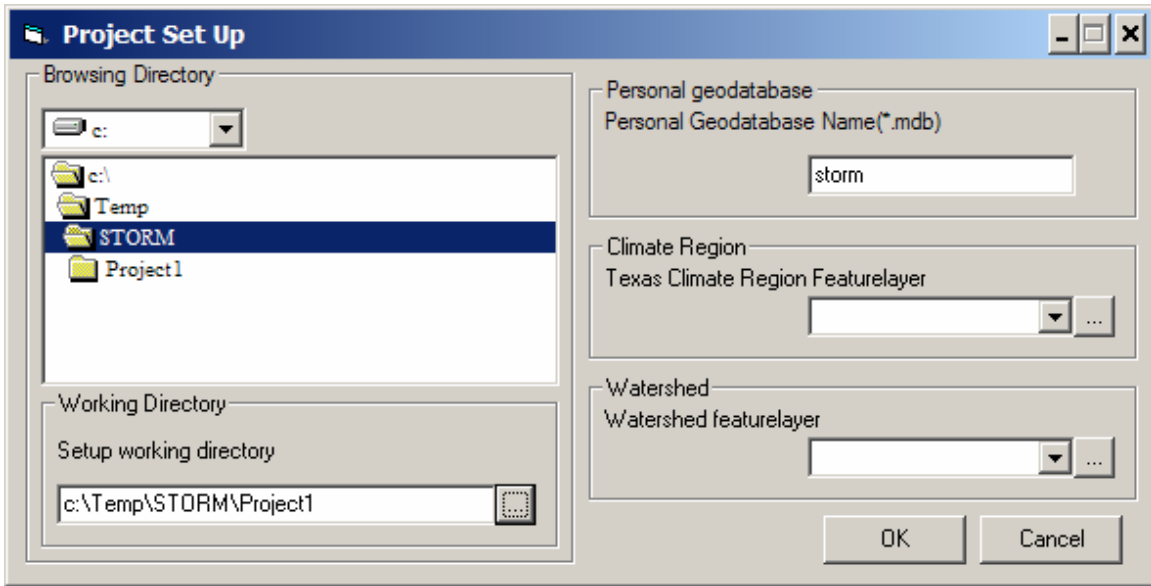


Figure 5.3: The Project Set Up Window.

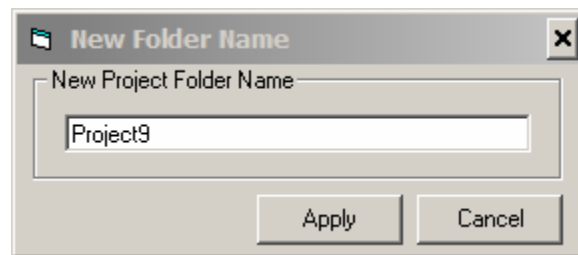


Figure 5.4: Project Folder Window.

Likewise, in the **Personal geodatabase** frame, enter the name of the geodatabase where your climate region and watershed data area are stored. In the **Climate Region** and **Watershed** frames, enter the names of the corresponding feature classes (Figure 5.5).

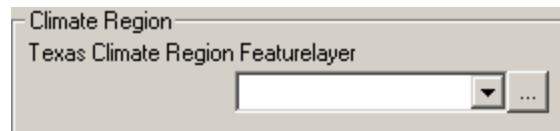



Figure 5.5: Climate Region Frame.

If any feature classes have already been added to the data frame, their names will appear in the comboxes. Also, you can load those feature classes from files by clicking on , which will open the browser window (Figure 5.6). When done, click **OK**.

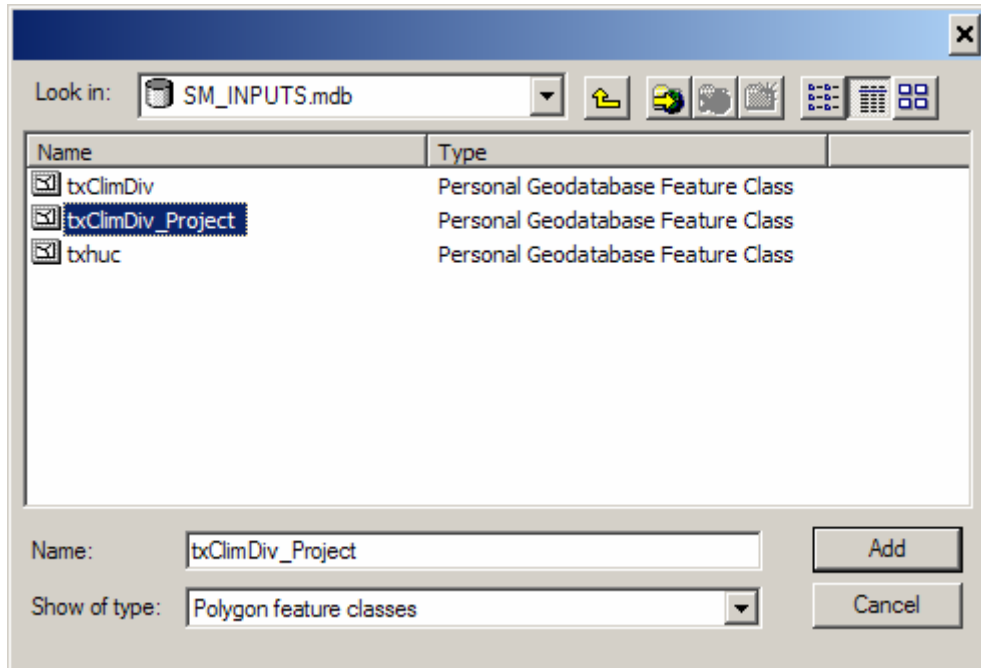


Figure 5.6: Open Feature Class of Climate Region for Texas.

SELECT WATERSHEDS

Click on **Project Setup/Select Watersheds** (Figure 5.7) and the **Select Watersheds** window pops up (Figure 5.8).

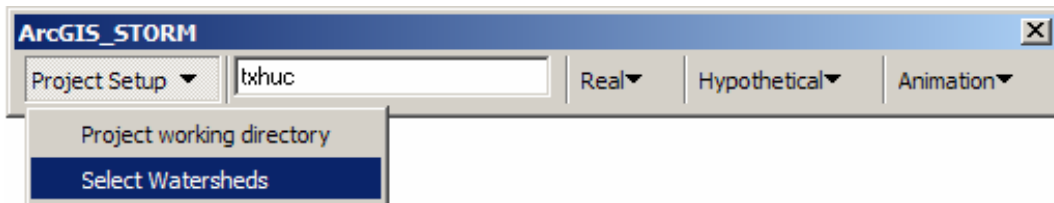


Figure 5.7: Select Watersheds Menu.

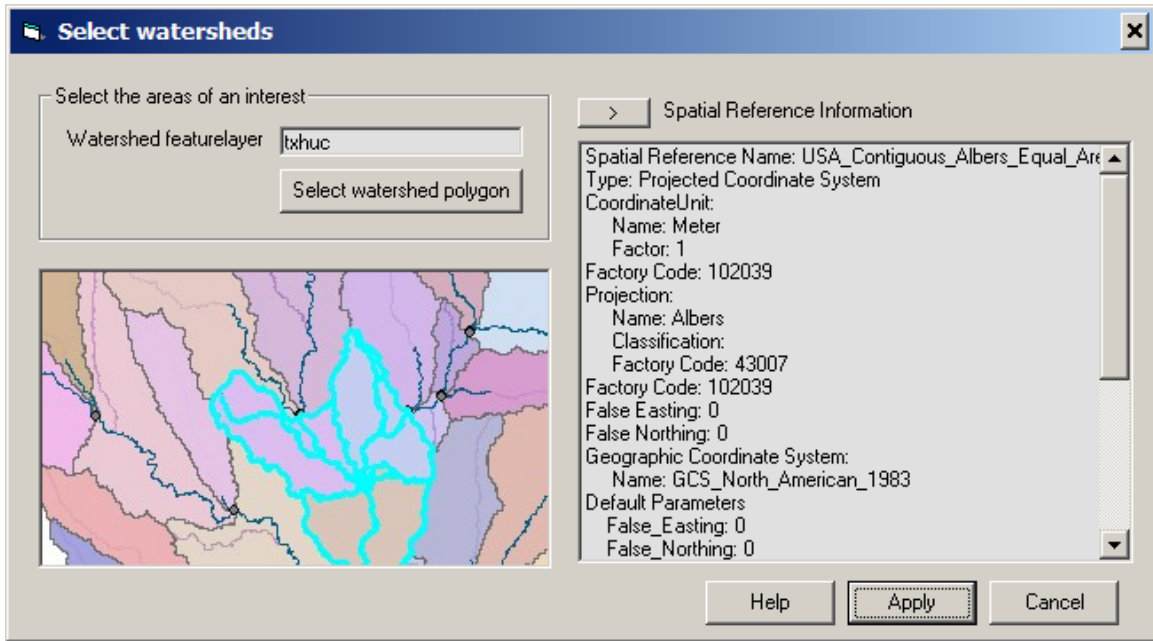


Figure 5.8: Select Watersheds Window.

In [Figure 5.8](#), the user begins by clicking on **Select watershed polygon** and selecting the watershed polygons of interest on the map ([Figure 5.9](#)). The number of watersheds should be less than 3. Once the watersheds are selected, click on **Apply**.

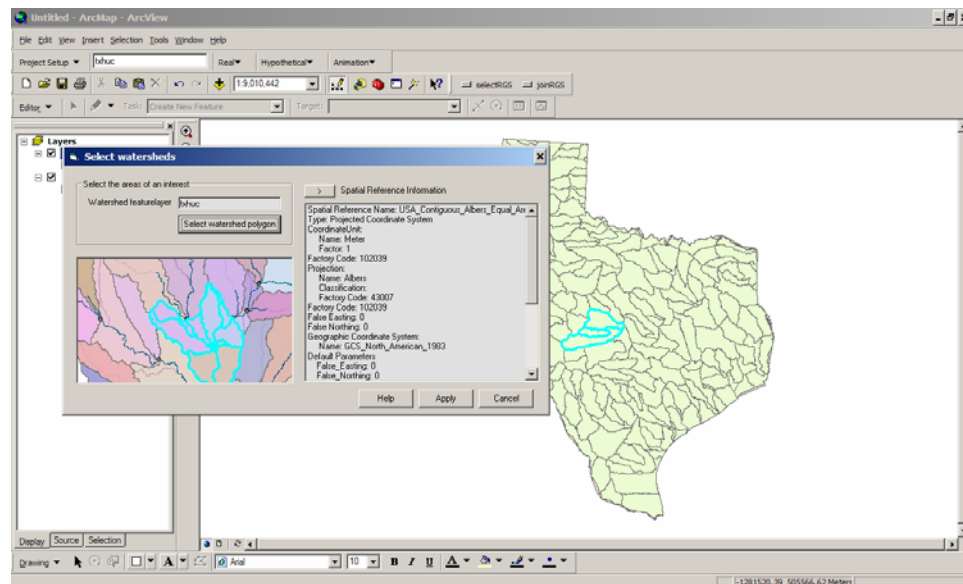


Figure 5.9: Example of Selecting Watersheds.

HYPOTHETICAL STORM

ArcGIS_STORM provides four different types of hypothetical storms, which, in the following, are called: FHS – Frequency-based Hypothetical Storm, SPS – Standard Project Storm, PMP – Probable Maximum Precipitation, and modPMP – modified Probable Maximum Precipitation (Figure 5.10).

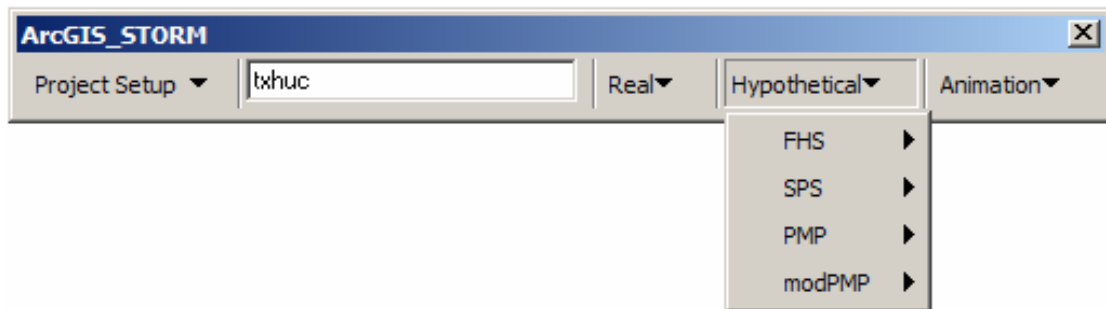


Figure 5.10: Hypothetical Storm Menu.

Frequency-Based Hypothetical Storm

Frequency-based hypothetical storms describe precipitation events based on a given exceedance probability for different durations. The procedure for determining the frequency-based hypothetical storm has four important elements:

- depth-duration-frequency curves (DDF curves),
- a standard isohyetal pattern,
- ARFs, and
- storm geometry (shape and orientation).

Click on **Hypothetical/FHS/Prepare storm inputs** (Figure 5.11) and the **Frequency-based Hypothetical Storm** window will pop up (Figure 5.12). In this window, different input data are added.

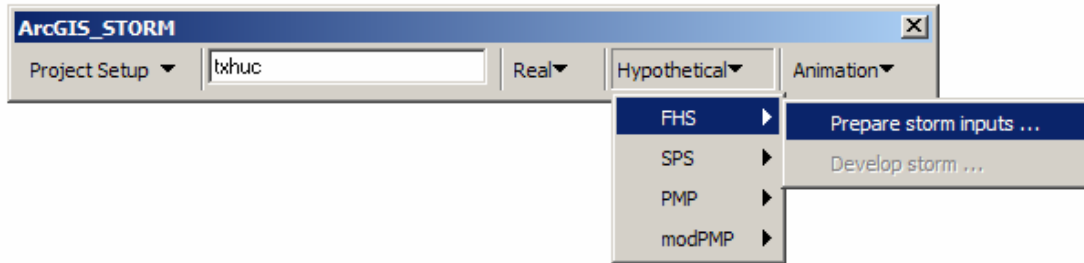


Figure 5.11: Hypothetical/FHS Menu.

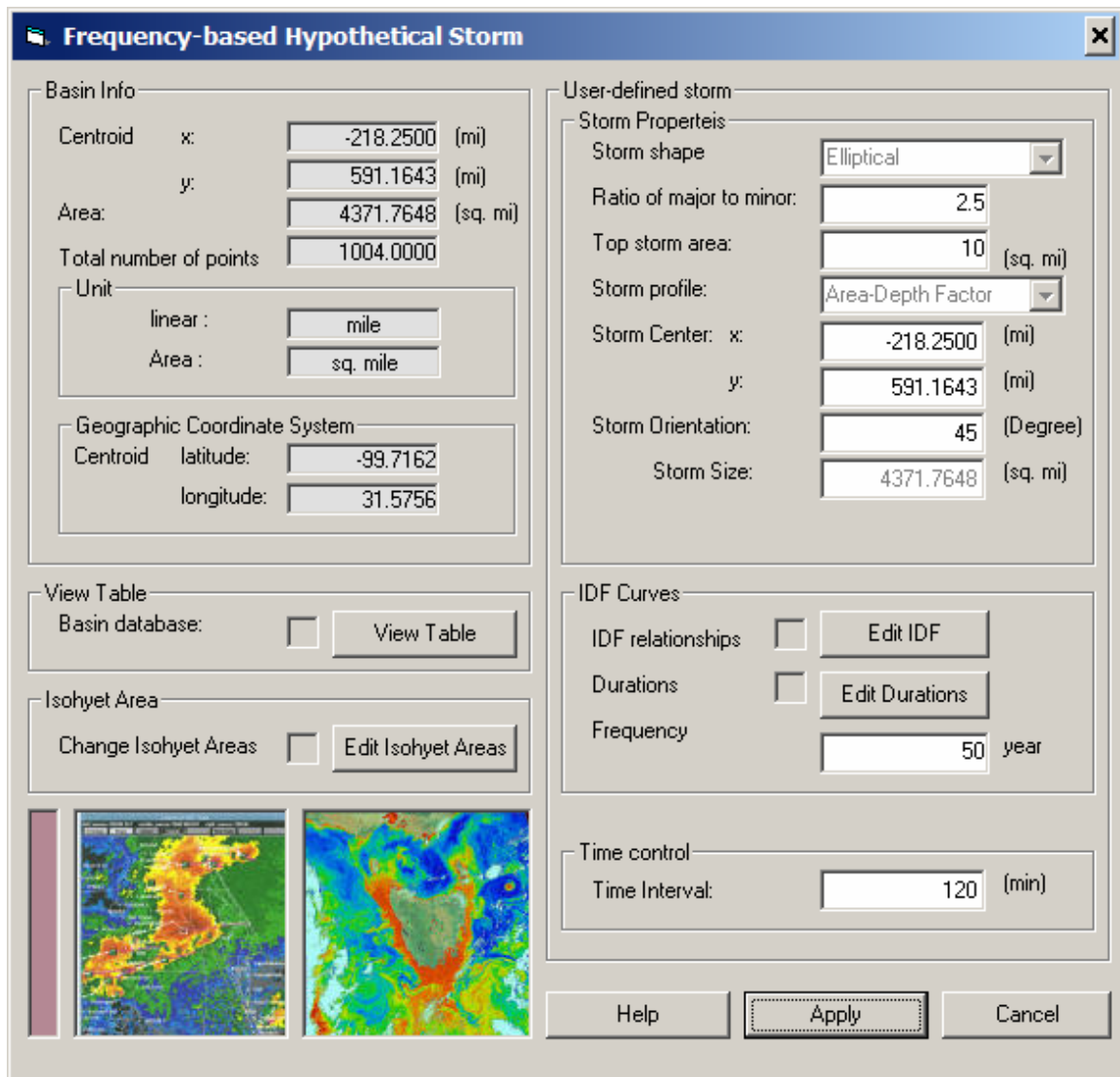


Figure 5.12: Input Storm Properties Window.

The storm properties for the development of a storm (Figure 5.13) are summarized as follows:

| Property Name | Description |
|-------------------------|---|
| Storm Shape | Elliptical shape (default). Currently only available option |
| Ratio of Major to Minor | Major axis length/minor axis length in an ellipse |
| Storm Center | x, y coordinates of the center of a storm |
| Storm Profile | Storm profile is a function of ARF |
| Storm Orientation | Angle between the major axis and the north direction. |
| Storm Size | Storm area that produces maximum precipitation on the basin |

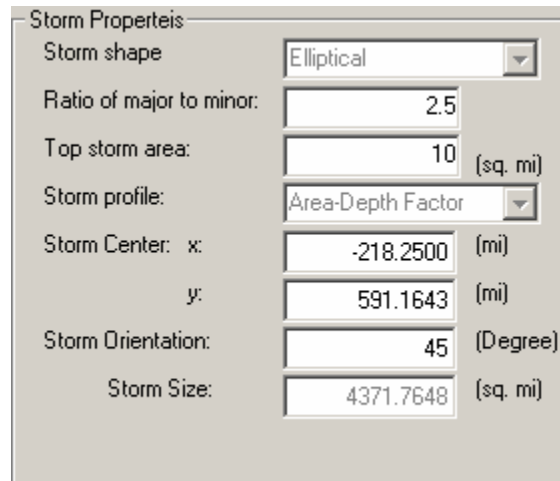


Figure 5.13: Storm Properties Window.

The tool also allows the user to set up IDF-curve coefficients (Figure 5.14).

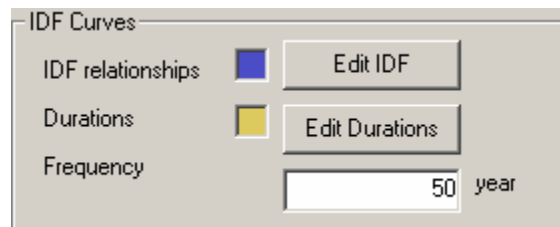


Figure 5.14: IDF Curves Window.

After clicking on **Edit IDF**, the user can specify the values of IDF curve coefficients (a, b or c) ([Figure 5.15](#)).

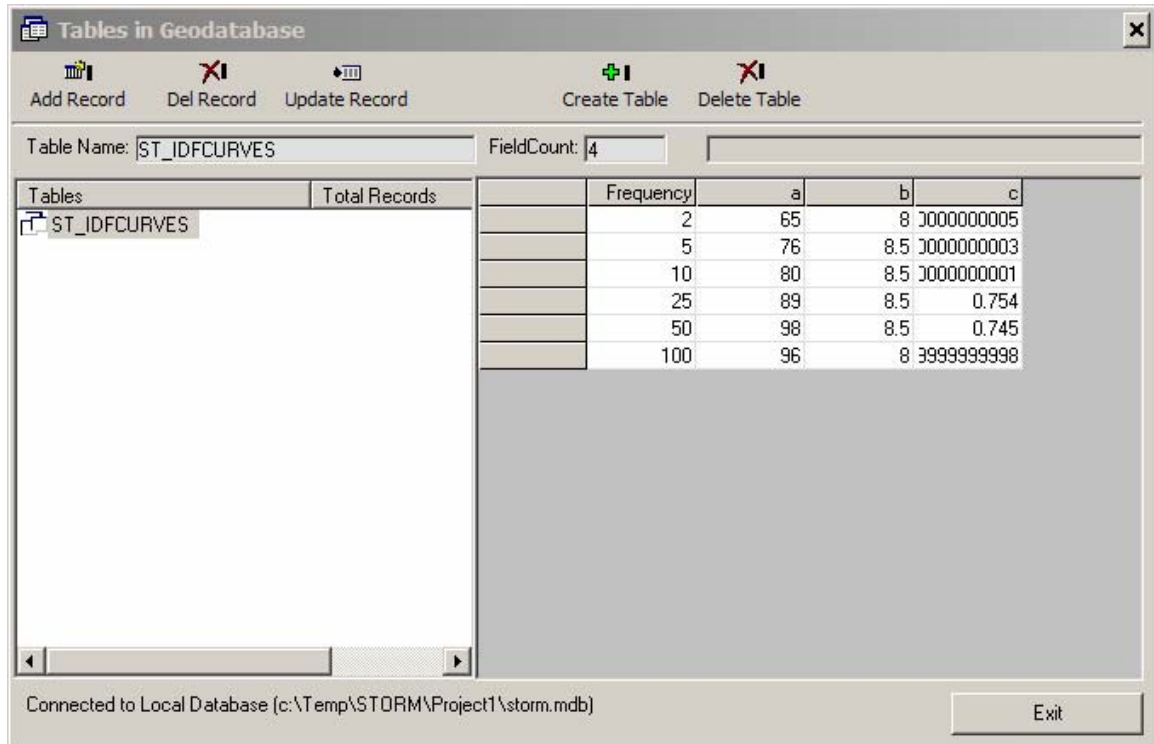


Figure 5.15: Edit IDF Curves Window.

After clicking on **Edit Durations** (see [Figure 5.12](#)), the user can modify the values of the durations. The default values are 1, 3, 6, 12 and 24 hrs ([Figure 5.16](#)).

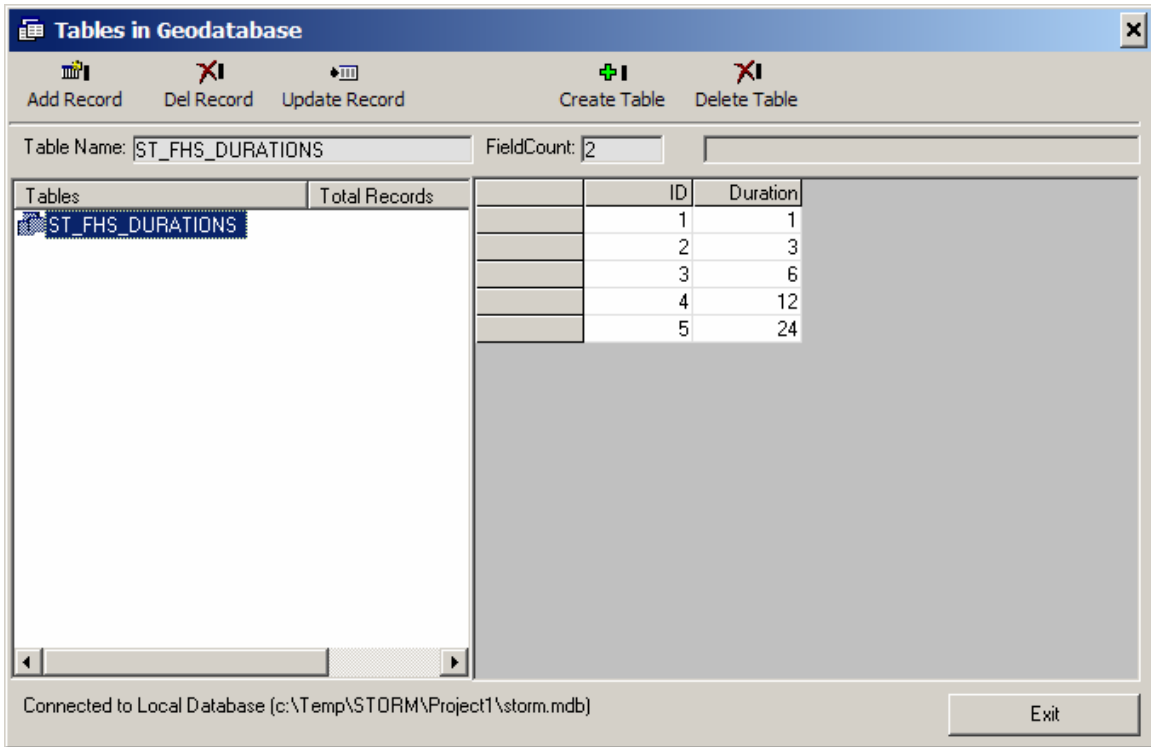


Figure 5.16: Edit Durations Window.

The user can specify the values of the isohyet areas by clicking on **Edit Isohyet Areas** in [Figure 5.12](#), which pops up the **Tables in Geodatabase** window ([Figure 5.17](#)). The default values are from 10 to 400 sq. mi.

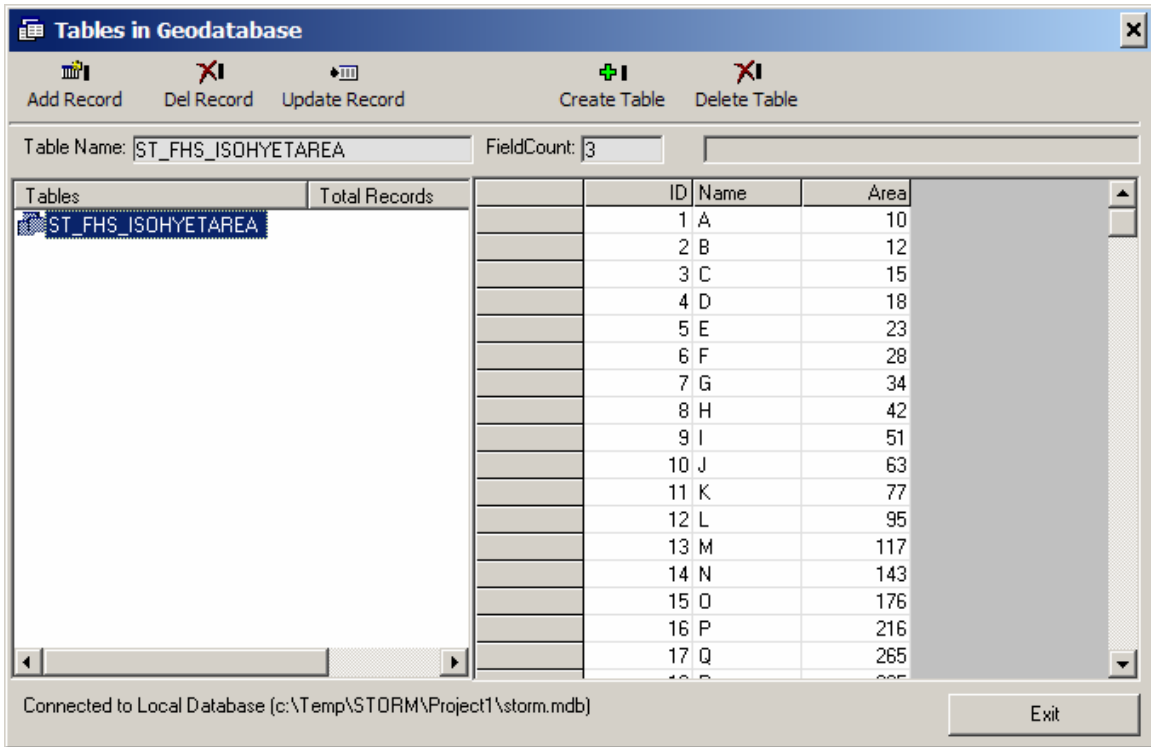


Figure 5.17: Edit Isohyet Area Window.

Once all input parameters have been set up, click on **Apply** in Figure 5.12, which will create and populate the geodatabase table ST_TAB.

To create a storm feature class and populate its attribute table, click on **Hypothetical/FHS/Develop storm** (Figure 5.18) and the **Developing Storm** window will pop up (Figure 5.19).

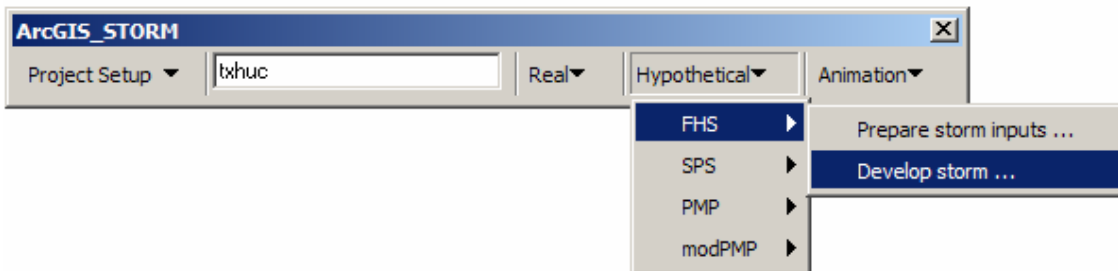


Figure 5.18: Develop Storm Menu.

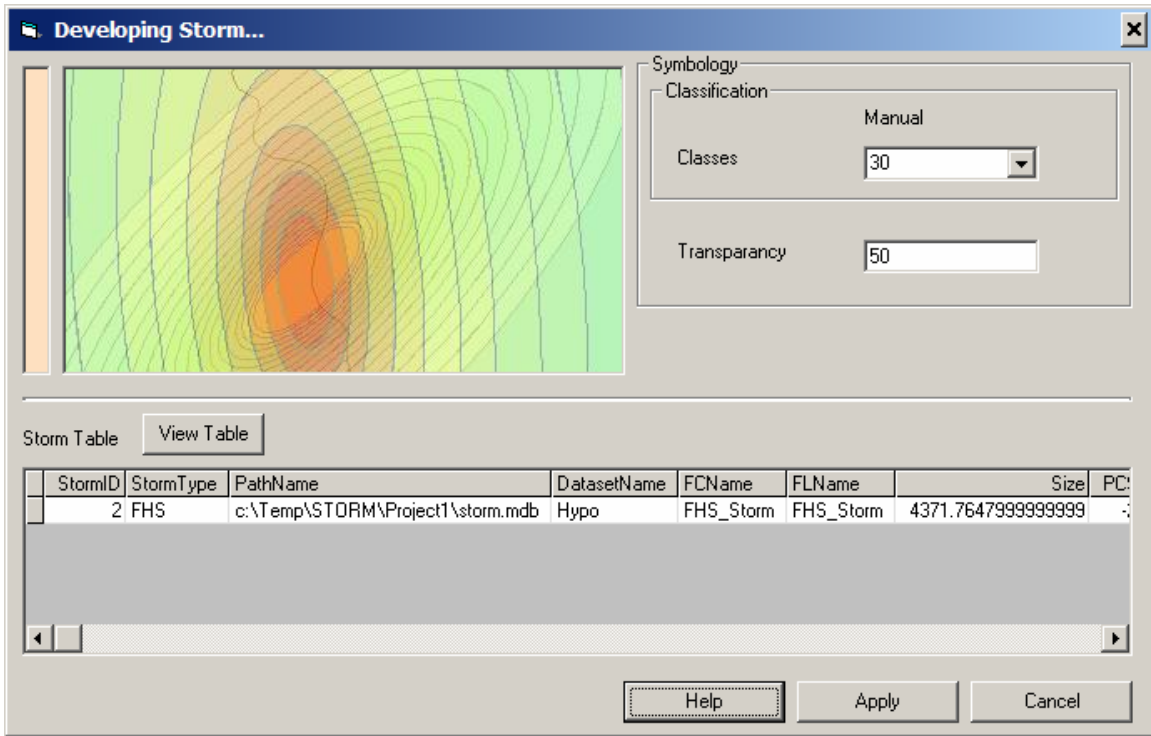


Figure 5.19: Developing Storm Window.

In this window, the user can specify the number of classes and transparency of the legend of the storm layer (Figure 5.20).

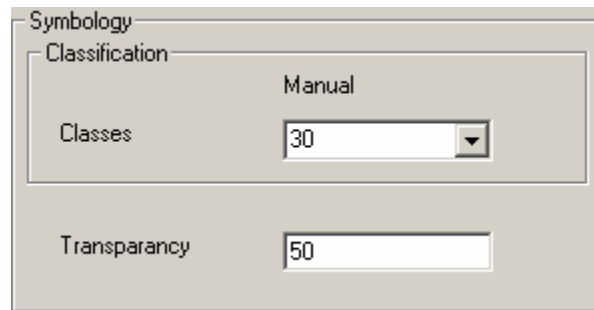


Figure 5.20: Symbology Setup.

To view the storm feature class attribute table (Figure 5.21), click on the **View Table** button.

| StormID | StormType | PathName | DatasetName | FCName | FLName | Size |
|---------|-----------|----------------|-------------|-----------|-----------|--------|
| 2 | FHS | c:\Temp\STO... | Hypo | FHS Storm | FHS Storm | 4371.7 |
| | | | | | | |
| | | | | | | |
| | | | | | | |
| | | | | | | |

Figure 5.21: Storm Feature Class Table.

In this attribute table, the fields are defined as follows:

| Field Name | Description |
|--------------|---|
| StormID | Unique storm identification number |
| StormType | Storm type: FHS, PMS or modPMS |
| PathName | Path name of the storm feature classes |
| DatasetName | Container of the storm feature classes: Hypo, Real |
| FCName | Feature class name |
| FLName | Feature layer name |
| Size | Storm size |
| PCSCntrX | Storm center x in projected coordinate system |
| PCSCntrY | Storm center y in projected coordinate system |
| Orientation | Storm orientation from north |
| Pref_Orient | preferred orientation determined by frequency of occurrence |
| ShapeRatio | Ratio of major axis/minor axis of the ellipse |
| TopArea | Topmost area of a storm |
| TimeInterval | Time interval for block design method |
| Frequency | Frequency for the determination of point rainfall depths |

Probable Maximum Storm (PMS)

This procedure will prepare an input text file for HMR52, and internally trigger HMR52 to calculate rainfall depths for each isohyet area for different durations and time intervals. It also

extracts storm information from the output text file created by HMR52 and creates a storm feature class. To trigger this option, click on **Hypothetical/PMP** (Figure 5.22).

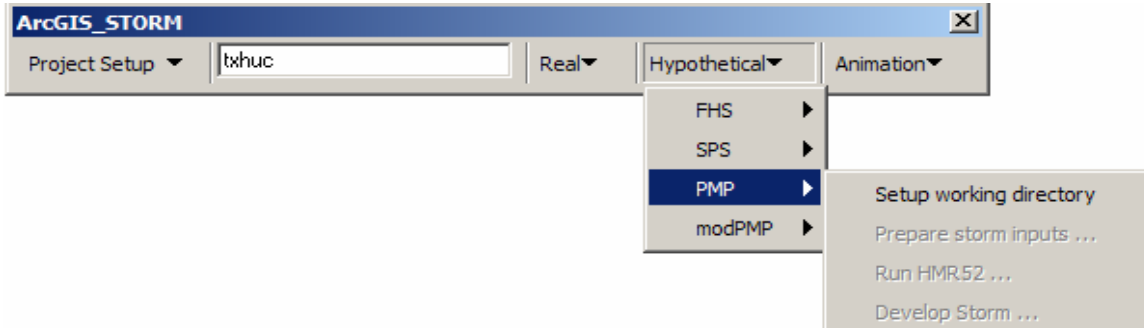


Figure 5.22: PMP Menu.

Before setting up the input parameters, the user has to specify the location of the HMR52 executable file and of a PMP geodatabase, which has PMP values and preferred storm orientations. Click on **Hypothetical/PMP/Setup working directory** (Figure 5.23) and the **PMP Project Setup** window will open (Figure 5.24).

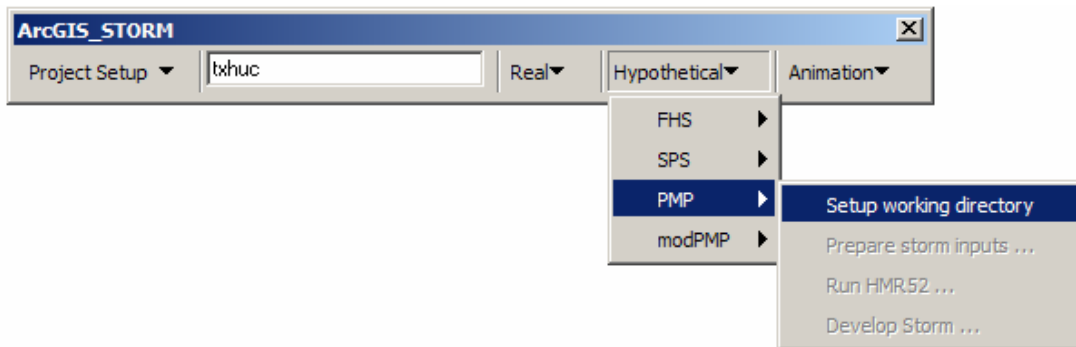


Figure 5.23: PMP Project Setup Menu.

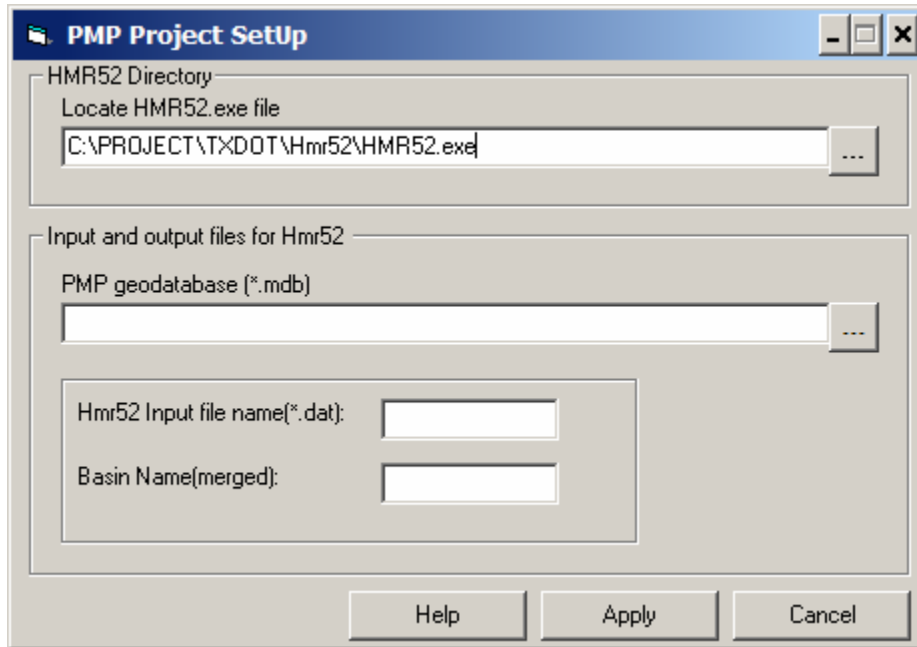


Figure 5.24: PMP Project Setup Window.

In the corresponding spaces, enter the path and file name of the HMR52 executable file and of the PMP geodatabase. If necessary, click on the button to the right of the space to browse the folder tree (Figures 5.25 and 5.26).

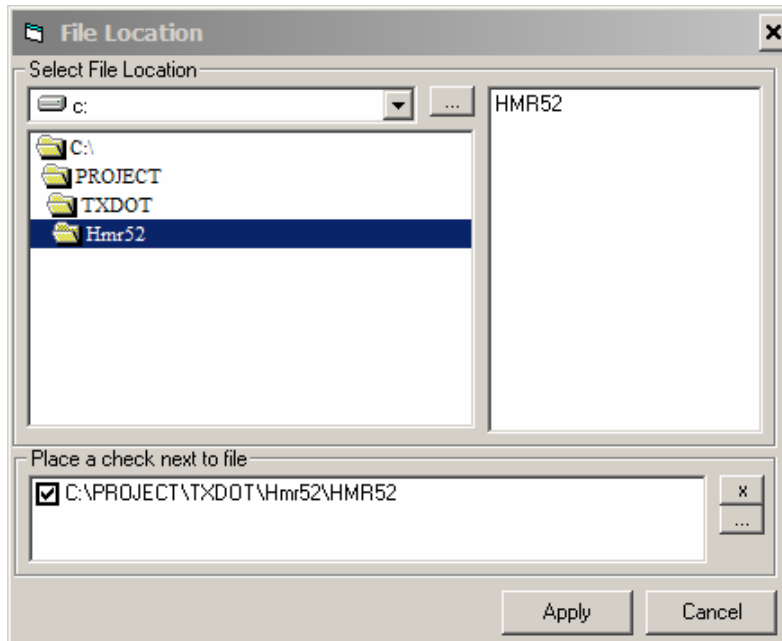


Figure 5.25: Location of the HMR52 Executable File.

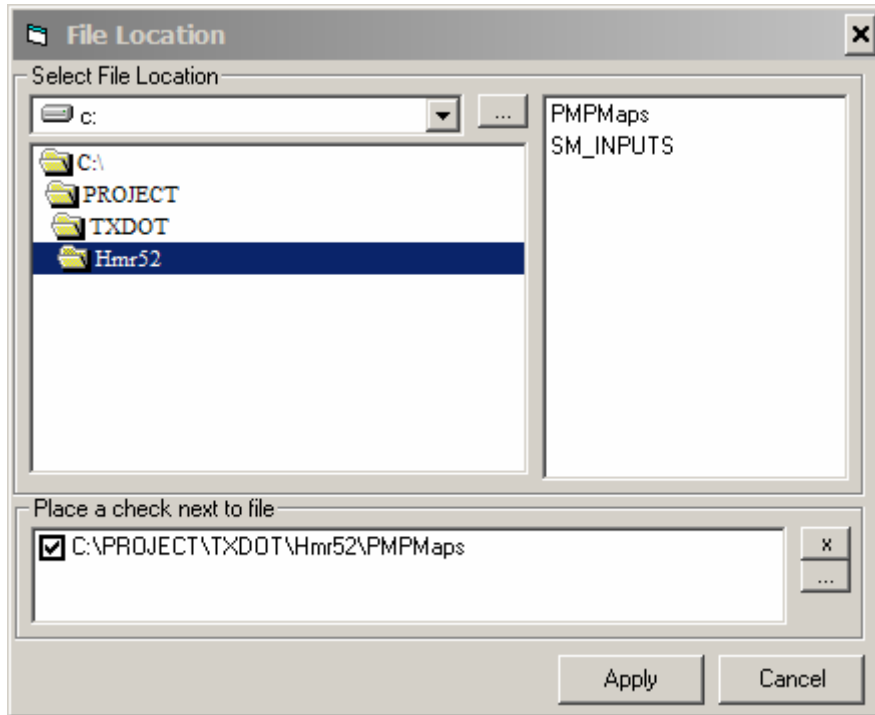


Figure 5.26: Location of the PMP Geodatabase.

Next, enter the HMR52 input file name and basin name (Figure 5.27).

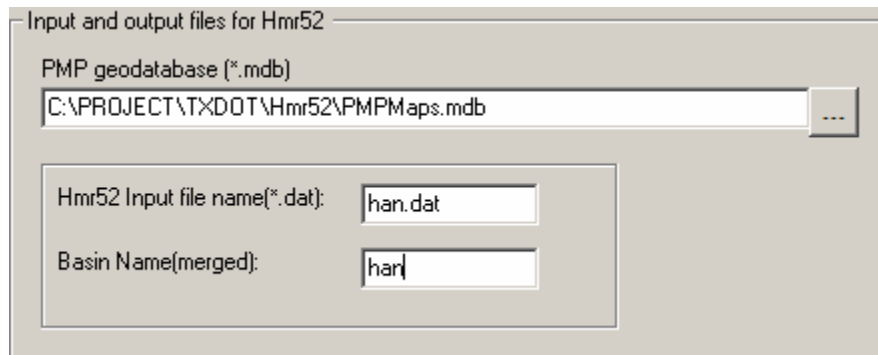


Figure 5.27: Input and Output File for HMR52.

To specify the storm geometry, orientation, duration, isohyet areas and time interval, click on **Hypothetical/PMP/Prepare storm inputs** (Figure 5.28) and the **Input Data** window will pop up (Figure 5.29).

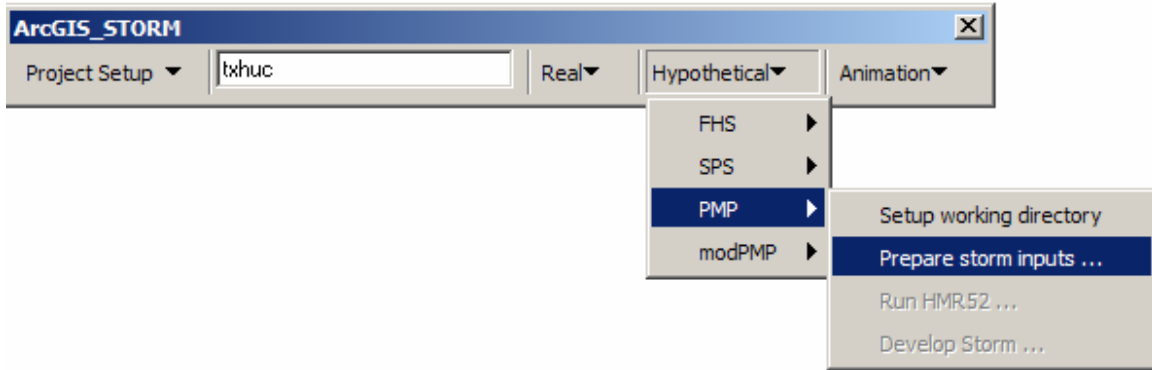


Figure 5.28: Prepare Storm Inputs Menu.

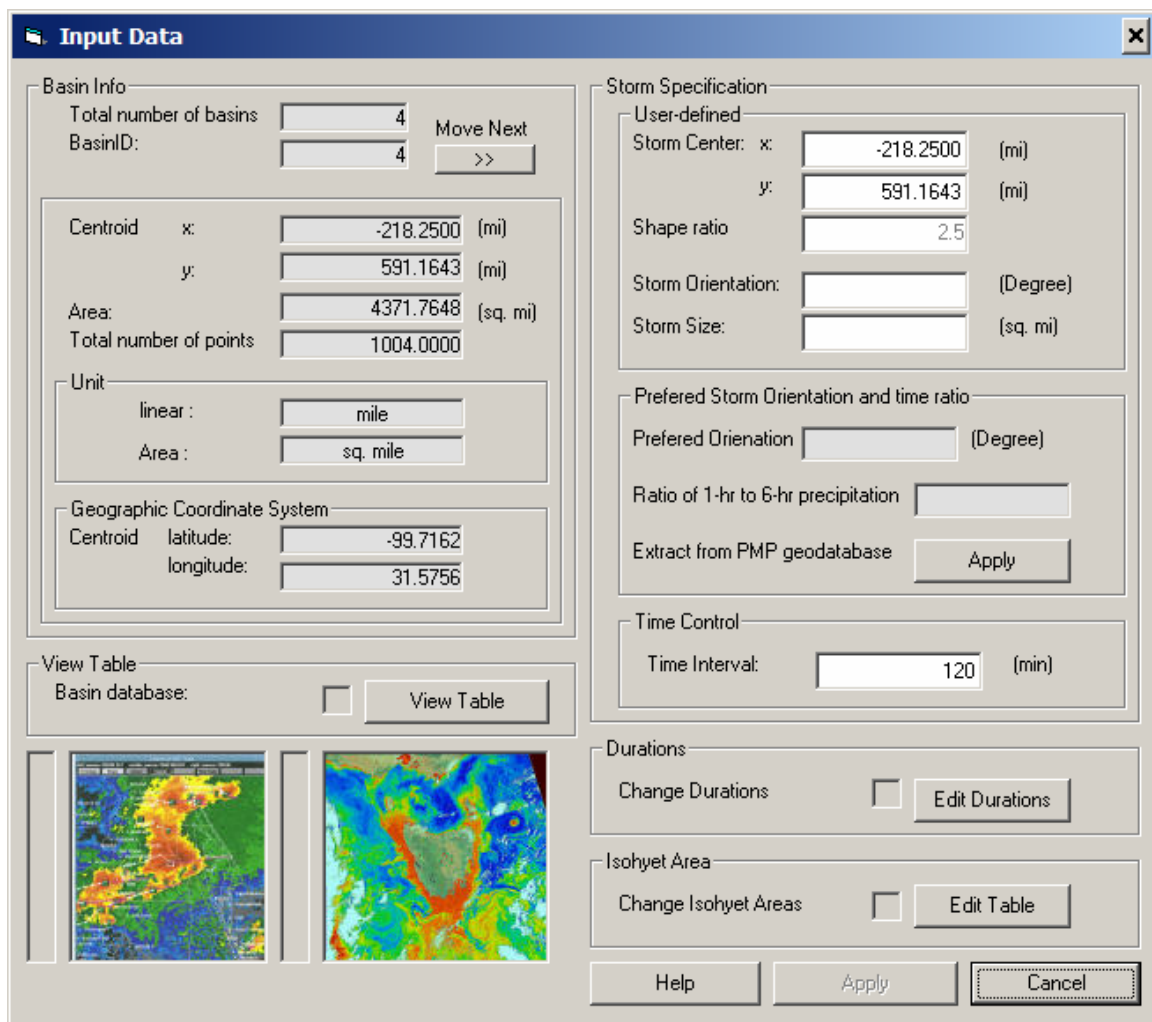


Figure 5.29: Input Data Window.

In the **Storm Specification/User-defined** frame (Figure 5.29), enter the storm properties as listed below. The shape ratio is fixed to 2.5 as default for PMP.

| Property Name | Description |
|----------------------|---|
| Storm Center | x, y coordinate of the center of the storm |
| Shape Ratio | Major axis/minor axis of the ellipse |
| Storm Orientation | Angle between the major axis and the north direction |
| Storm Size | Storm-area size which produces maximum precipitation on the basin |

In the **Storm Specification/Preferred Storm Orientation and time ratio** frame (Figure 5.29), enter the information according to the table below and click on **Apply**, and it will automatically extract information from the PMP geodatabase for the geographic location of the storm.

| Property Name | Description |
|-------------------------------------|--|
| Preferred Orientation | Preferred orientation provided by HMR52 |
| Ratio of 1-hr to 6-hr Precipitation | The 6-hr increments may be distributed into shorter intervals based on the ratio |

After the storm area and orientation have been determined, the HMR52 program calculates the precipitation temporal distribution for durations up to 72 hrs. Incremental precipitation for a user-defined time interval is calculated. In the **Storm Specification/Time Interval** space (Figure 5.29), enter the time interval.

Likewise, in the **Durations** frame (Figure 5.29), the user can edit the durations of the hyetograph blocks by clicking on the **Edit Durations** button and revising the **ST_PMP_DURATIONS** table in the **Tables in Geodatabase** window that pops up (Figure 5.30).

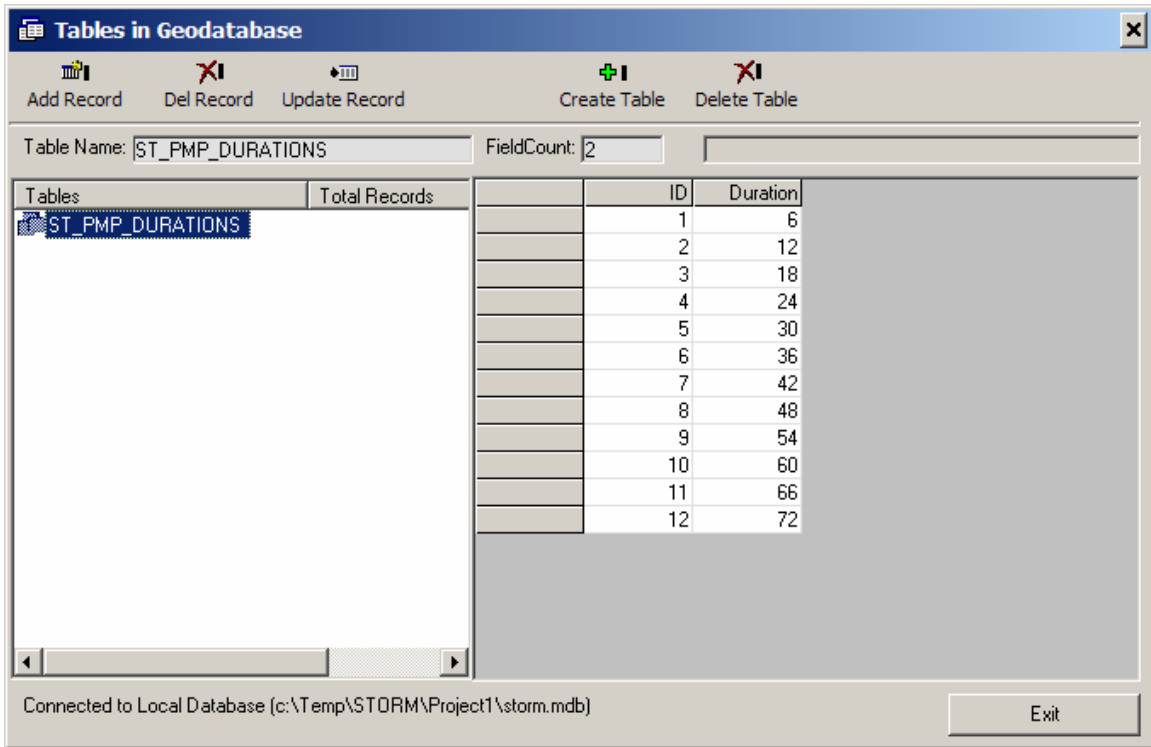


Figure 5.30: Edit Durations Window.

Similarly, in the **Isohyet Area** frame (Figure 5.29), the user can edit the area of the isohyets by clicking on the **Edit Table** button and revising the **ST_PMP_ISOHYETAREA** table in the **Tables in Geodatabase** window that pops up (Figure 5.31).

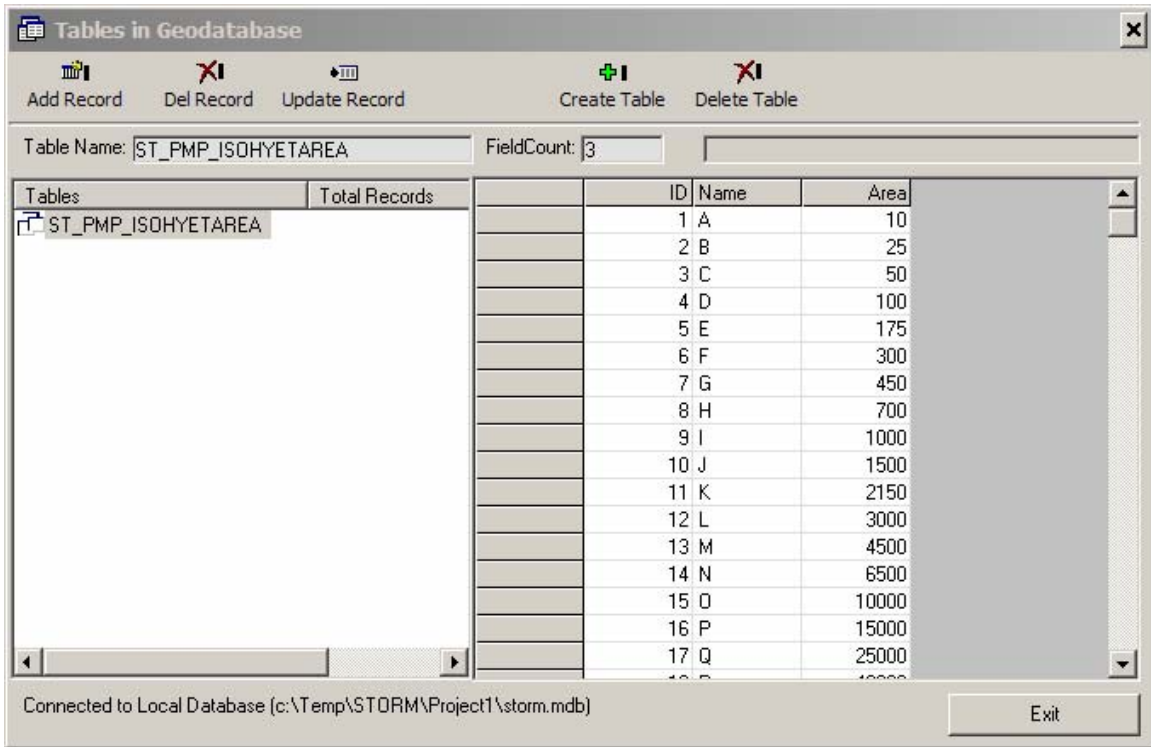


Figure 5.31: Edit Isohyet Areas Window.

By clicking on the **View Table** button in the **View Table** frame in [Figure 5.29](#), the user can see information about the selected basin features and the dissolved basin which is obtained from the selected ([Figure 5.32](#)).

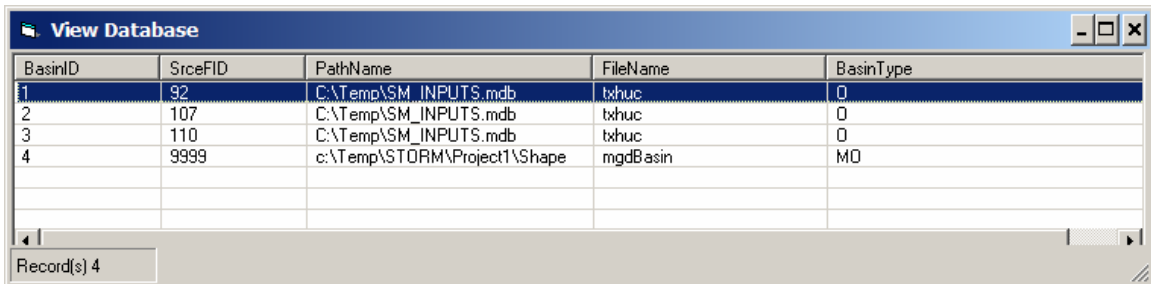


Figure 5.32: Basin Table.

The field names of basin tables are as follows:

| Field Name | Description |
|------------|------------------------------------|
| BasinID | Unique basin identification number |
| SrceFID | Source feature ID |
| PathName | Path name for source feature class |
| FileName | Source feature class name |
| BasinType | Basin type: O, MO |

This is the procedure to run HMR52 and to create a data file containing the incremental basin-average precipitation values for every subbasin requested and their dissolved basin. To trigger it, click on **Hypothetical/PMP/Run HMR52** (Figure 5.33) and the **Execute HMR52** window will pop up (Figure 5.34).

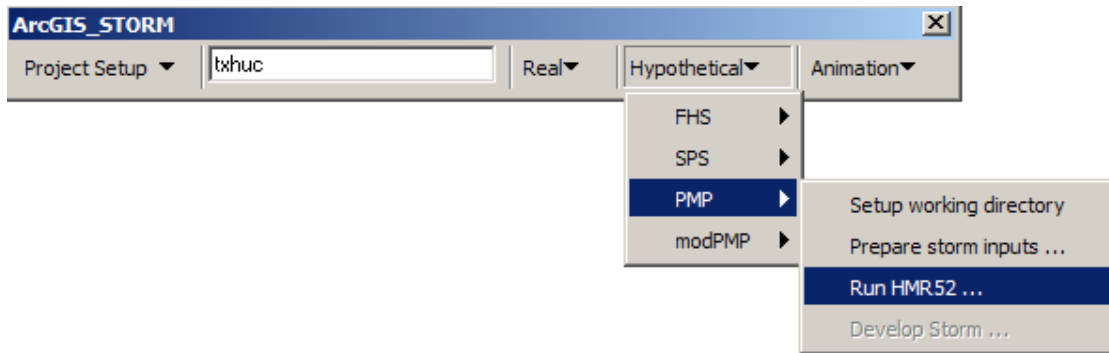


Figure 5.33: Run HMR52 Menu.

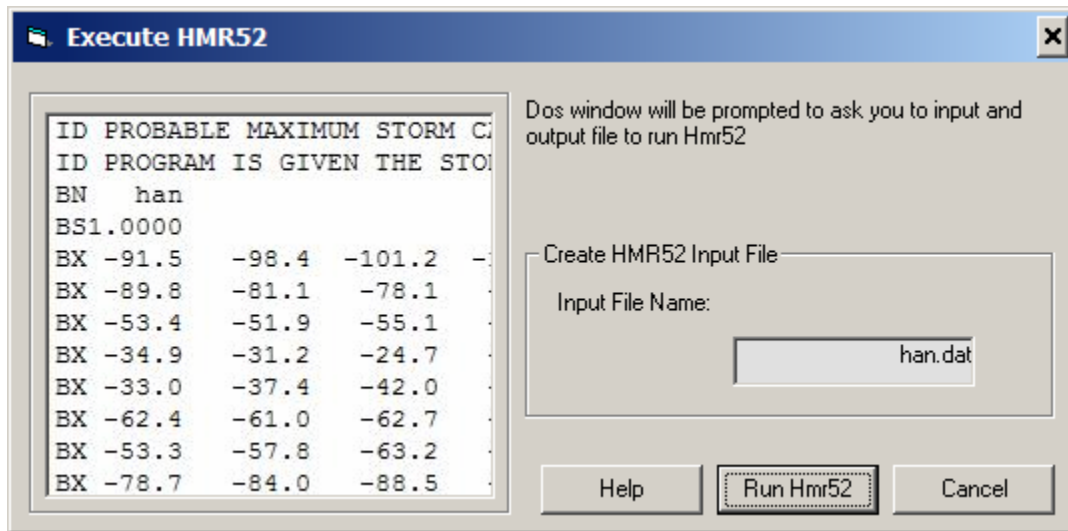


Figure 5.34: Execute HMR52 Window.

Once the user clicks on the **Run HMR52** button, a Disk Operating System (DOS) window will be prompted to ask the user to enter input and output file for HMR52 subsequently.

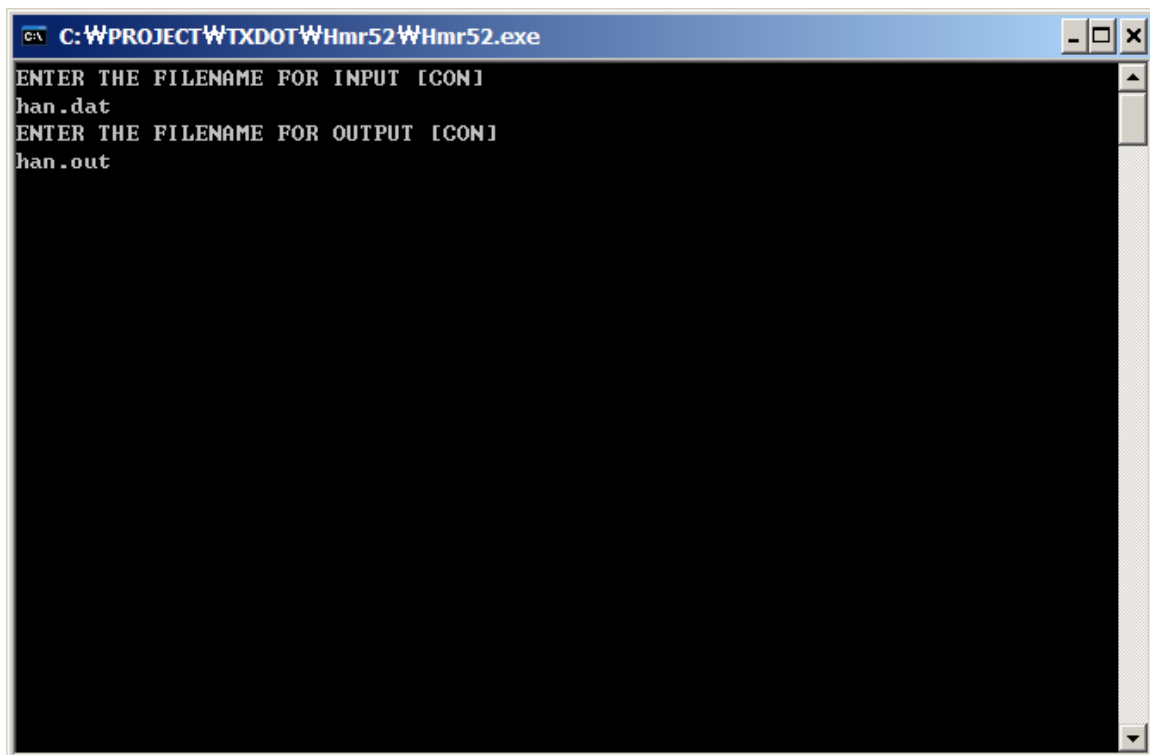


Figure 5.35: HMR52 DOS Window.

The program extracts storm properties and incremental basin-average precipitation values from HMR52, and creates a storm feature class that includes that information. To trigger this capability, click on **Hypothetical/PMP/Develop Storm** (Figure 5.36) and the **Developing Storm** window will pop up (Figure 5.37).

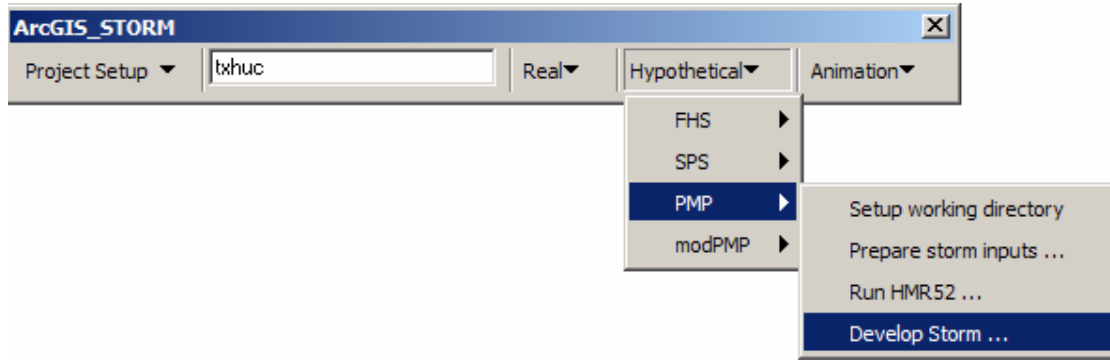


Figure 5.36: Develop Storm Menu.

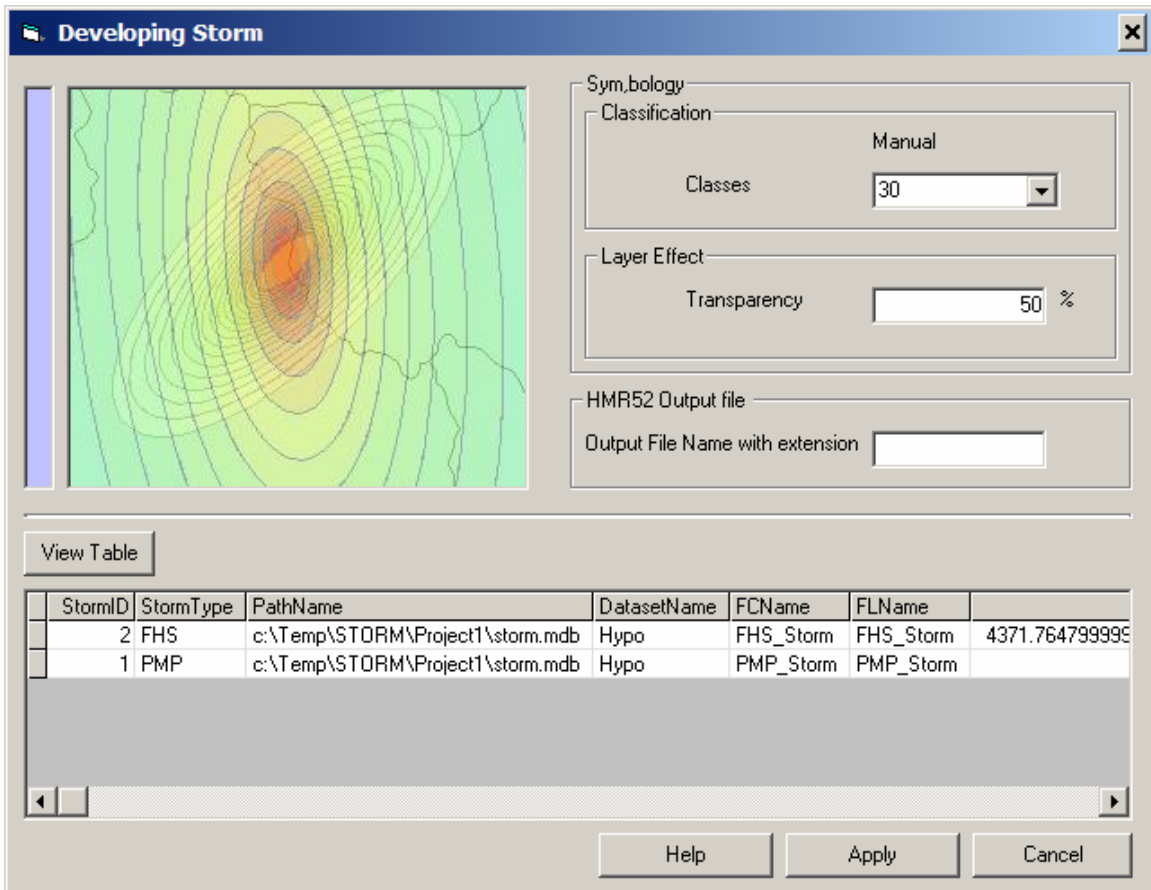


Figure 5.37: Developing Storm Window.

In the **Symbology** frame (Figure 5.37), the user can specify the number of classes and transparency of the storm feature layer. In the **HMR52 Output file** frame (Figure 5.37), the user also has to enter the name of the HMR52 output file. The program will use storm information from this data file to create a storm feature class.

As soon as the user clicks on **Apply**, the program draws ellipses based on storm information obtained from user inputs and the information file created by HMR52. It calculates the accumulated rainfall depths for each of the enclosed areas shown in Figure 5.38. Figure 5.39 shows the corresponding attribute table of the storm feature class.

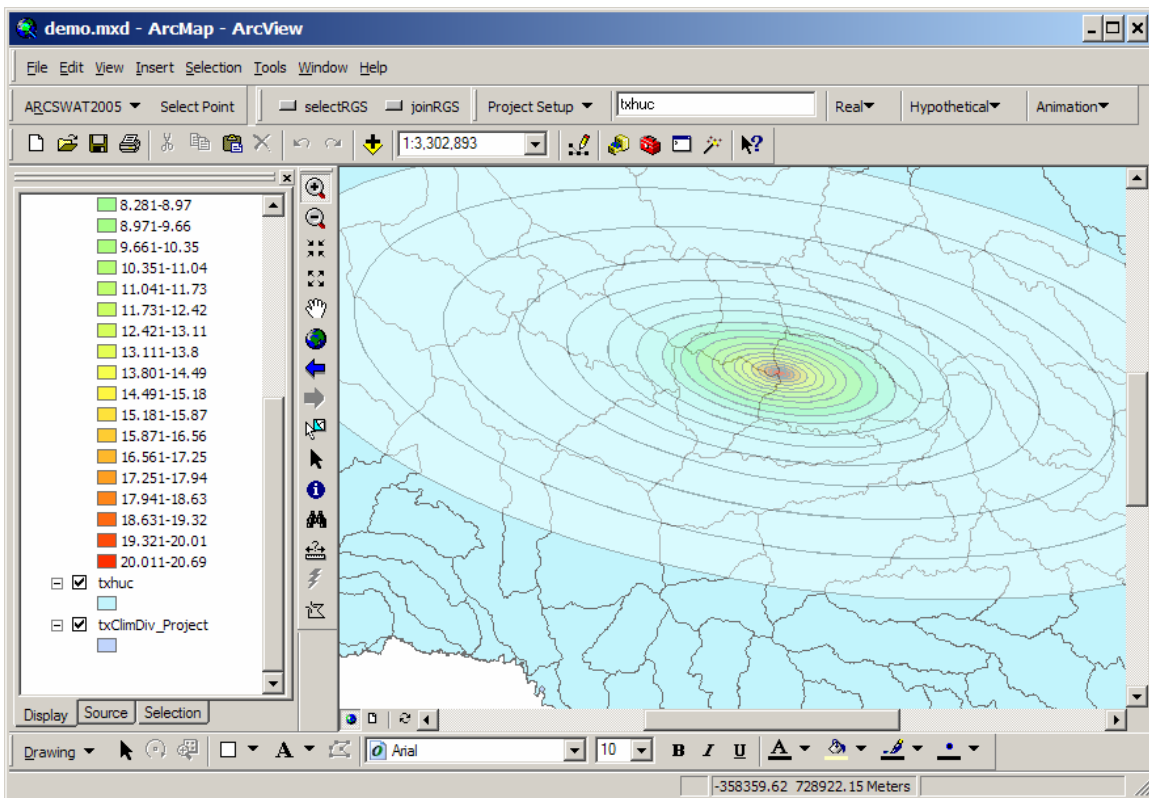


Figure 5.38: PMP Storm.

| OBJECTID | Shape | Shape_Len | Shape_Area | EnclosedArea | D_6_hr | D_12_hr | D_18_hr | D_24_hr | D_30_hr | D_36_hr | D_42_hr | D_48_hr | D_54_hr | D_60_hr | D_66_hr | D_72_hr |
|----------|---------|-------------|-------------|--------------|--------|---------|---------|---------|---------|---------|---------|---------|---------|---------|---------|---------|
| 1 | Polygon | 20894.44852 | 25899881.10 | 10 | 20.69 | 4.93 | 2.71 | 1.87 | 1.47 | 1.21 | 1.02 | 0.89 | 0.79 | 0.71 | 0.64 | 0.58 |
| 2 | Polygon | 53931.72660 | 38110916.40 | 25 | 19.42 | 4.76 | 2.68 | 1.87 | 1.47 | 1.21 | 1.02 | 0.89 | 0.79 | 0.71 | 0.64 | 0.58 |
| 3 | Polygon | 79758.81868 | 63269823.77 | 50 | 18.14 | 4.63 | 2.65 | 1.87 | 1.47 | 1.21 | 1.02 | 0.89 | 0.79 | 0.71 | 0.64 | 0.58 |
| 4 | Polygon | 112795.9643 | 126543509.1 | 100 | 16.86 | 4.51 | 2.63 | 1.87 | 1.47 | 1.21 | 1.02 | 0.89 | 0.79 | 0.71 | 0.64 | 0.58 |
| 5 | Polygon | 153483.8083 | 189072462.2 | 175 | 15.58 | 4.42 | 2.61 | 1.87 | 1.47 | 1.21 | 1.02 | 0.89 | 0.79 | 0.71 | 0.64 | 0.58 |
| 6 | Polygon | 201856.2130 | 323748513.7 | 300 | 14.31 | 4.34 | 2.6 | 1.87 | 1.47 | 1.21 | 1.02 | 0.89 | 0.79 | 0.71 | 0.64 | 0.58 |
| 7 | Polygon | 254815.8817 | 375178086.9 | 450 | 13.41 | 4.23 | 2.59 | 1.87 | 1.47 | 1.21 | 1.02 | 0.89 | 0.79 | 0.71 | 0.64 | 0.58 |
| 8 | Polygon | 314989.6841 | 626795654.4 | 700 | 12.26 | 4.17 | 2.58 | 1.87 | 1.47 | 1.21 | 1.02 | 0.89 | 0.79 | 0.71 | 0.64 | 0.58 |
| 9 | Polygon | 383772.1734 | 747402317.0 | 1000 | 11.24 | 4.09 | 2.58 | 1.87 | 1.47 | 1.21 | 1.02 | 0.89 | 0.79 | 0.71 | 0.64 | 0.58 |
| 10 | Polygon | 464862.8804 | 1250593998. | 1500 | 10.22 | 4.02 | 2.57 | 1.87 | 1.47 | 1.21 | 1.02 | 0.89 | 0.79 | 0.71 | 0.64 | 0.58 |
| 11 | Polygon | 562300.2683 | 1627773168. | 2150 | 7.15 | 3.18 | 2.09 | 1.51 | 1.19 | 0.98 | 0.83 | 0.72 | 0.64 | 0.57 | 0.52 | 0.47 |
| 12 | Polygon | 668303.5393 | 2112689180. | 3000 | 5.24 | 2.55 | 1.69 | 1.22 | 0.96 | 0.79 | 0.67 | 0.58 | 0.52 | 0.48 | 0.42 | 0.38 |
| 13 | Polygon | 805174.7803 | 3768361475. | 4500 | 3.32 | 1.9 | 1.33 | 0.96 | 0.75 | 0.62 | 0.53 | 0.46 | 0.41 | 0.36 | 0.33 | 0.3 |
| 14 | Polygon | 975985.5446 | 5179976220. | 6500 | 2.04 | 1.31 | 0.98 | 0.71 | 0.56 | 0.46 | 0.39 | 0.34 | 0.3 | 0.27 | 0.24 | 0.22 |
| 15 | Polygon | 1193497.045 | 8768955693. | 10000 | 0.89 | 0.72 | 0.62 | 0.45 | 0.35 | 0.29 | 0.25 | 0.21 | 0.19 | 0.17 | 0.15 | 0.14 |
| 16 | Polygon | 1470041.290 | 12505938301 | 15000 | 0 | 0 | 0 | 0 | 0 | 0 | 0 | 0 | 0 | 0 | 0 | 0 |
| 17 | Polygon | 1854039.497 | 25159875176 | 25000 | 0 | 0 | 0 | 0 | 0 | 0 | 0 | 0 | 0 | 0 | 0 | 0 |
| 18 | Polygon | 2366303.641 | 37665811480 | 40000 | 0 | 0 | 0 | 0 | 0 | 0 | 0 | 0 | 0 | 0 | 0 | 0 |
| 19 | Polygon | 2940082.553 | 51799762206 | 60000 | 0 | 0 | 0 | 0 | 0 | 0 | 0 | 0 | 0 | 0 | 0 | 0 |

Figure 5.39: PMP Storm Table.

Modified PMP

The modified PMP option differs from the PMP option in that the ratio of the major axis length to the minor axis length can be user defined. Thus, the modified PMP option is flexible in terms of the storm shape. To open this option, click on **Hypothetical/modPMP** (Figure 40). The window for the input data is similar to the one for PMP.

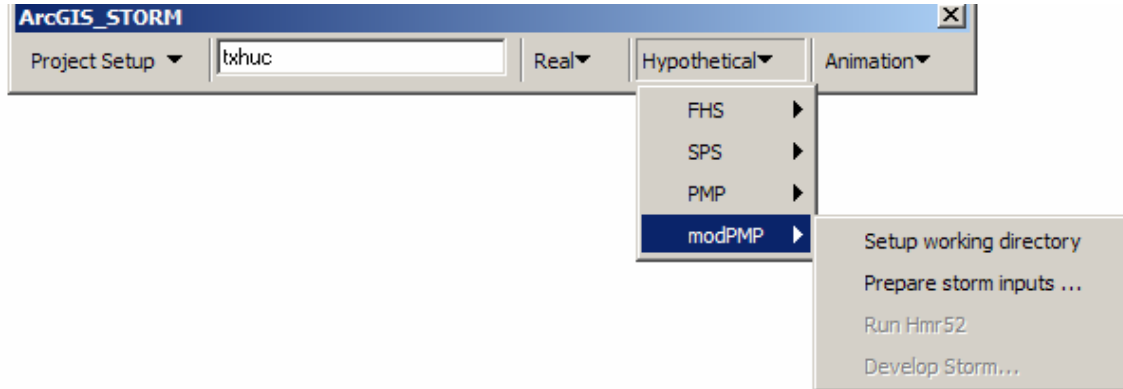


Figure 5.40: Modified PMP Menu.

Animation

The program creates and displays an animation of the storm showing the changes in rainfall depths over time. To trigger this option, click on **Animation/Open Animation Control** (Figure 5.41) and the **Animation** window pops up (Figure 5.42).

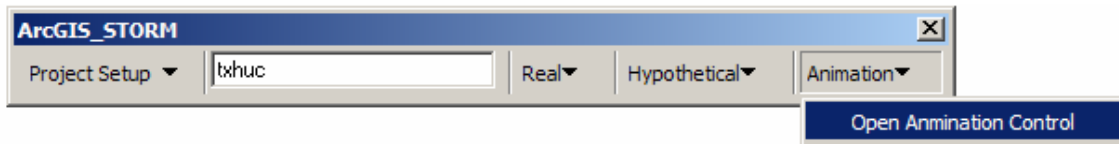


Figure 5.41: Animation Toolbar.

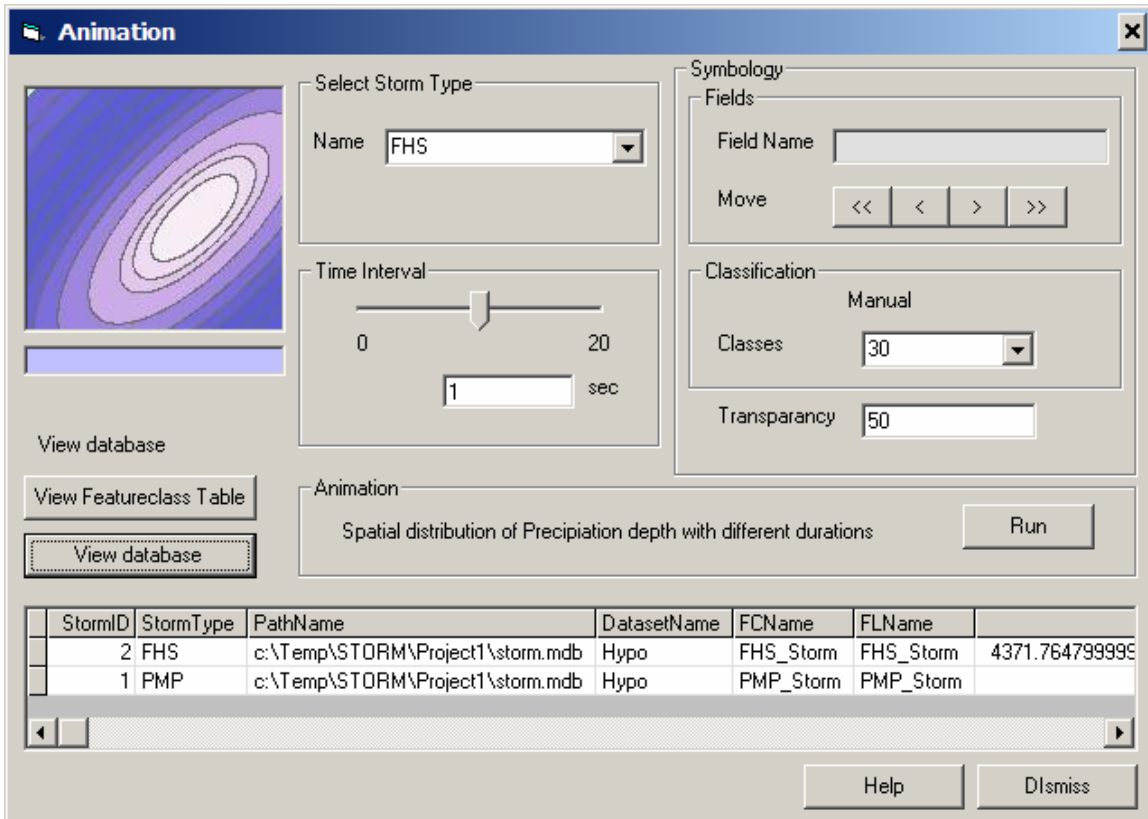


Figure 5.42: Animation Setup Window.

6. MOVING STORMS

Understanding the storm's properties is important for developing a hypothetical storm that captures its geometric and dynamic characteristics. This hypothetical storm can then be used as input for hydrologic modeling because rainfall is distributed in space and time. The geometric pattern of a storm is critical to understanding the rainfall-runoff process in a hydrologic system. Some relevant geometric and dynamic properties of a storm are its shape, area, centroid location, and direction and speed of movement. These properties would be difficult to capture with current rain gauge data, which are too sparse to accurately capture the spatial aspects of a storm. However, with the advent of NEXRAD rainfall data, it is believed that such properties can be captured. Storm identification, tracking and analysis studies have been conducted in the past using pattern recognition, cross-correlation and other techniques (Dixon and Wiener 1993). These techniques, however, are developed for the forecasting of convective storms having a short duration.

In earlier studies with radar-based precipitation data with a time step shorter than an hour, individual storm cells were identified, tracked and trended (Dixon and Wiener 1993). However, no research has been conducted for the case of data with a time step longer than 1 hr. Once rainfall is accumulated, the overall characteristics of a storm may be dramatically changed. However, even though accumulating data will likely result in losing some detailed information, it is possible to obtain some meaningful patterns out of the accumulated rainfall data. It is difficult to identify storm cells that last less, for example, than 30 minutes using hourly data and computational methods; therefore, it would not be possible to implement the same type of analysis used when short time step data are available. In our study, a new methodology is presented that relies on a geometric approach to identify the shape and orientation of a given storm. This methodology utilizes the hierarchical clustering of imaged objects (i.e., storm cells), according to the shapes of their boundaries, and identifies a representative two-dimensional geometric shape of the storm. Image analysis is carried out to identify the geometric properties of the storms in the temporal and spatial domain, and a contour method is used to segment and identify a storm. Once these properties are identified and categorized, they can be used to develop a representative hypothetical storm. Stage III rainfall data were used to develop hypothetical storms. Storm identification is the first step to develop a dynamic storm.

Rainfall fields consist of storms, rain bands, rain clusters and rain cells in a hierarchical pattern. Storms consist of rain bands, which move in the same direction as the storm. Rain bands consist of rain clusters and isolated rain cells. Rain clusters consist of rain cells arranged in a clustered form, and move perpendicular to the direction of movement of the rain bands. Rain cells are born, grow, decay and die in a short period compared to rain bands; show a stochastic behavior; and move in a common direction, but their direction is not the same as a storm (Figure 6.1).

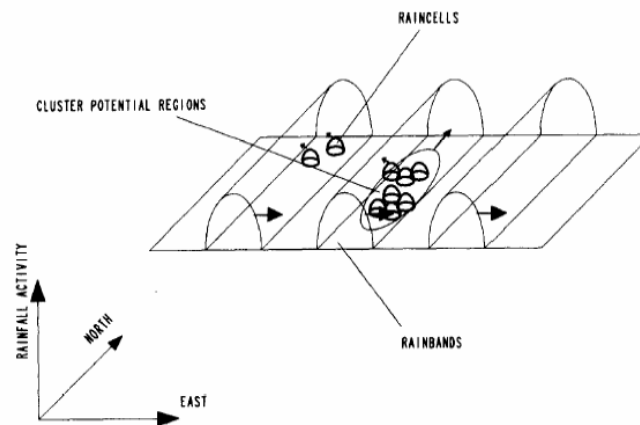


Figure 6.1: Aspects of Frontal Rainstorms (Mellor 1996).

STORM SYSTEM IDENTIFICATION AND TRACKING (SSIT) ALGORITHM

The methodology presented here provides the framework necessary to identify a storm and its structure using hourly NEXRAD data. In addition, it allows one to develop static and dynamic hypothetical storms. Image analysis is utilized to segment and identify the storm structure. Once the storm structure and its geometric and dynamic properties are identified and categorized, they can be used for developing static and dynamic storms. The steps required in the development of a hypothetical dynamic storm are summarized in Figure 6.2.

Object detection is used to segment and identify storm objects. This segmentation of storm objects is carried out by taking advantage of the difference in contrast between background, representing no rainfall regions, and objects, representing storm bands, clusters or cells.

The *Sobel* method (Figure 6.3) creates a binary mask with a specified threshold. The threshold is set to detect changes in contrast, thus defining the outline of the rainfall pattern. The binary gradient mask is dilated to eliminate the gaps between lines and fill the holes in the storm structure. The storms on the border need to be removed for calculation efficiency. The segmented storm can be obtained by smoothing boundaries.



Figure 6.3: Image Process by the Sobel Method.

Rainfall of weak intensity may be considered noise. If the noise is not eliminated, one might end up including many storm objects, which are not important. Therefore, it is reasonable to use a gradient mask to remove the noise and detect a storm’s boundary using a specific threshold value. This method might be useful to identify mesoscale storms since the cells that have weak intensity would be removed (Figure 6.4).

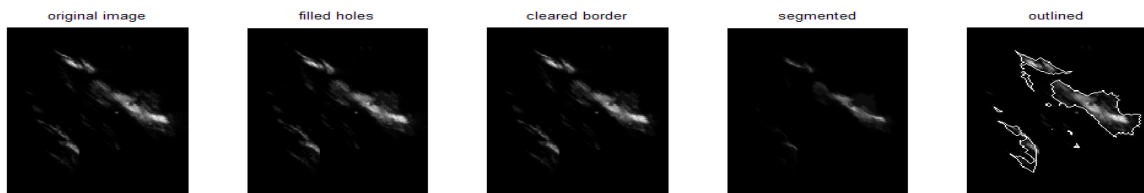


Figure 6.4: Image Process by Eliminating Noise.

The *Canny* algorithm (Figure 6.5), known as the optimal edge detector, is used to segment storm objects. Noise is filtered out using a Gaussian filtering method. After that, the Sobel operator performs a two-dimensional spatial measurement to calculate the gradient. Hysteresis reduces the gradient array, created by the Sobel operator, by tracking along the pixels.

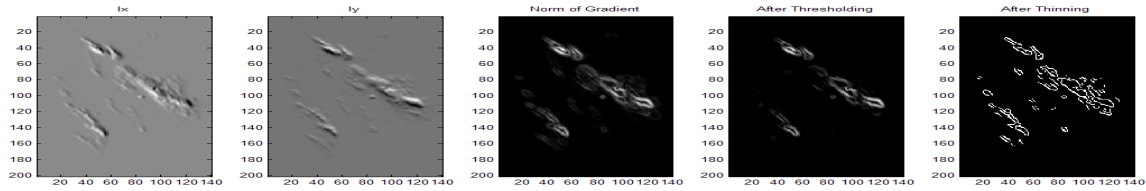


Figure 6.5: Image Process Using the Canny Algorithm.

The *contour* method is used to segment the storm object based on contour lines. By changing a rainfall threshold value, it is possible to segment and identify a storm, rain bands, rain clusters or rain cells according to the density of rainfall in a given area (Figure 6.6).

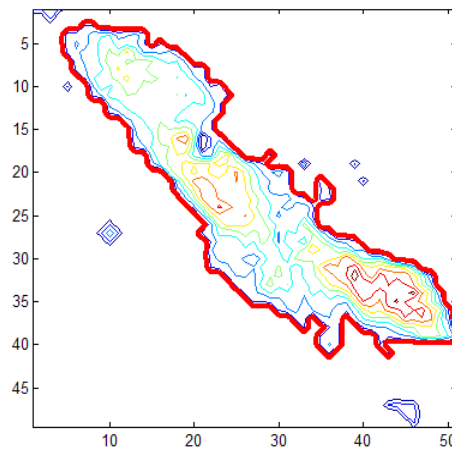


Figure 6.6: Segmentation by a Contour Line.

The contour method will be used in the following because of its simplicity.

Labeling Objects

The next step is to label the storm objects to get properties such as area, orientation and representative elliptical shape, which is obtained using the principal component analysis (PCA). The images in Figure 6.7 are obtained by labeling objects created by different segmentation methods.

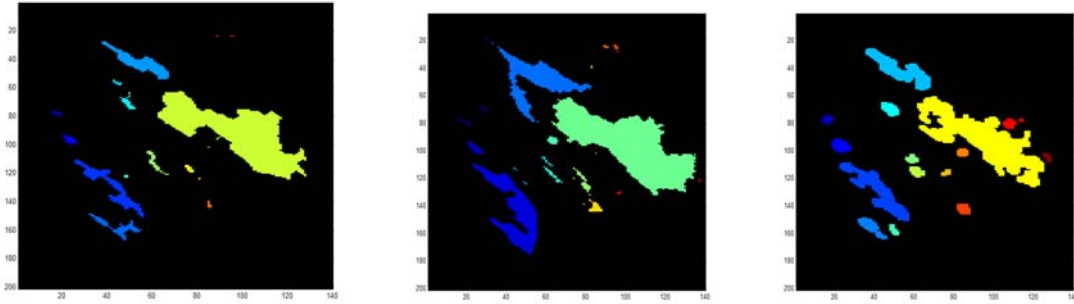


Figure 6.7: Labeled Objects.

Storm System

Figures 6.8, 6.9 and 6.10 illustrate how different thresholds are used to identify the hierarchical structure of a storm. The algorithm changes the rain threshold to find storm objects within a storm until the number of contours increases by one. The biggest storm objects, called rain bands, would be identified first. Once rain bands are identified, rain clusters within rain bands are searched, identified and segmented. Finally, rain cells within a rain cluster are searched and segmented. The following figures show the process of extracting the hierarchical storm structure. Rain bands, rain clusters and rain cells are categorized based on the measure of their longest dimension (Rigo and Llasat 2002).

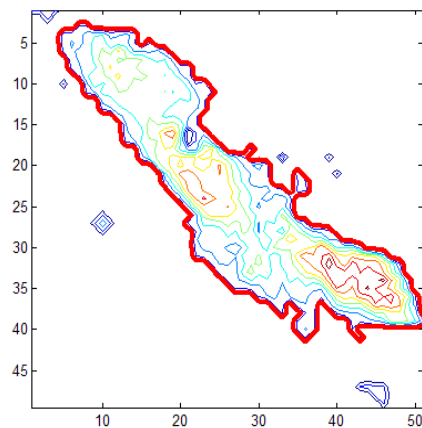


Figure 6.8: Mesoscale Convective Systems or Rain Bands (Longest Dimension > 100 km).

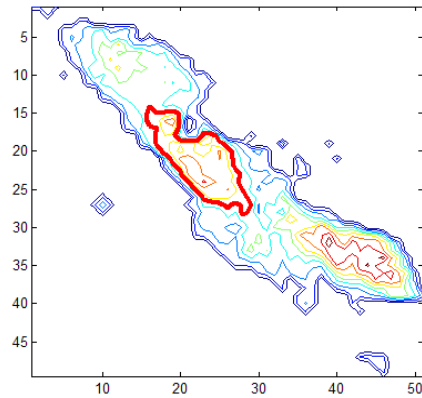


Figure 6.9: Multicell Storms or Rain Cluster (Longest Dimension < 100 km).

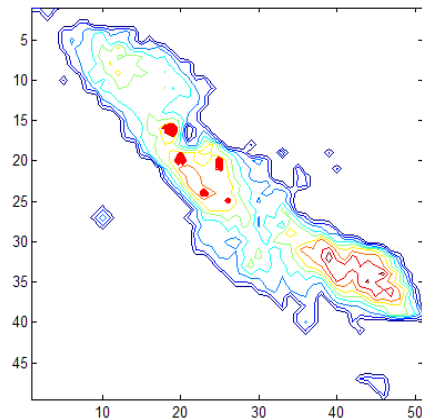


Figure 6.10: Rain Cells (Longest Dimension \approx 5 km).

Storm Tracking

Once a storm is identified, its geometric properties are calculated. The geometric properties can be centroid location, orientation and ratio of major axis length to minor axis length when a storm is represented as an ellipse. The storm can then be matched in terms of similarity of properties to other past storms. A function, representing a degree of similarity, would be used to locate the storm at a later time, and determine the direction and speed of motion.

Storm Data Model

The storm data model (Figure 6.11) is designed to be incorporated and used with ESRI ArcGIS object models. All the properties of a storm will be saved in this standard format.

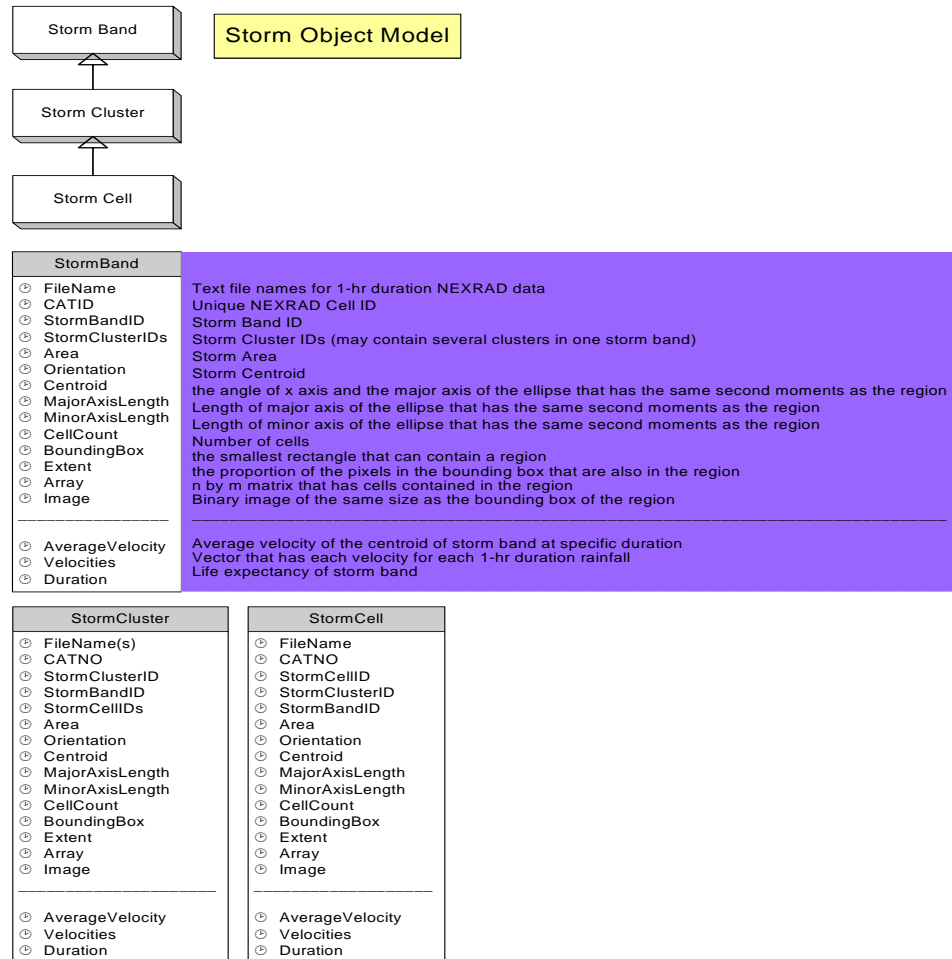


Figure 6.11: Storm Data Model.

7. CONCLUSIONS

In general, “larger catchments are less likely than smaller catchments to experience high intensity storms over the whole of the catchment area” (Siriwardena and Weinmann 1996). Therefore, the conversion of point precipitation into area-averaged precipitation is necessary whenever an area, large enough for rainfall not to be uniform, is to be modeled. However, while point precipitation has been well studied because of the availability of rain gauge data, areal precipitation cannot be measured, and its estimation has been a subject of research for the last decades. In this report, the estimation of the ratios of areal average precipitation to point precipitation (i.e., ARFs) using radar precipitation data is studied. The study site is the 685,000-km² area covered by the state of Texas.

ARFs were calculated for different regions of Texas, storm durations, storm areas, precipitation depths, storm shapes and orientations, and seasons. Because the anisotropy of the storm field was an important matter of study, the storm-centered ARF calculation method was used. Likewise, because of the continuous improvements to the NEXRAD algorithms, which cause the data not to be homogeneous over time, only data for years 2003 and 2004 were considered. This lack of long-term historical data prevented any type of frequency analysis and, instead, ARFs were related to rainfall depths for given durations (which correspond to specific return periods). On the other hand, the analysis was based on thousands of storm events that took place in the 2-year period in the study area.

For each storm duration (i.e., 1, 3, 6, 12 and 24 hrs), geographic region (see Figure 4.3) and precipitation depth quartile (i.e., 25%, 50%, 75% and 100%), regression equations were determined for the ARF values as a function of area. It was found that the ARFs showed a decay tendency with the increase of area according to

$$\text{ARF} = 1 - c A$$

for areas less than 45 km² and

$$\text{ARF} = a \log (A) + b$$

for areas greater than 45 km², where a, b and c are constants that vary with region, duration and depth, and the area is in km². The values of a, b and c were given in Tables 4.1 to 4.5 of Chapter 4, for the different durations and regions. Whenever it was found that the depth quartiles were not statistically different, the regression curves were collapsed. It was observed that the regression equations were clearly different for the different regions. Likewise, according to the

depth-duration-frequency curve concept, depth and frequency are related for a given duration. So, since it was observed that the ARFs increased with depth, it was concluded that they also increase with return period.

Histograms of the aspect of the ellipses that represented the storms suggest that around one-third of the ellipses had an aspect between 1 and 2, which corresponds to almost-circular shapes. The remaining two-thirds of the storms had a clear elliptical shape with an aspect greater than 2. It was also observed that the frequency decreased as the aspect increased. Overall the same patterns were observed for the different regions and durations. Likewise, histograms of the orientation angle show a clear predominance of a 45° angle for regions 3, 5 and 6, which was stronger for the shorter durations than for the longer durations (specially for region 6). Note that regions 3 and 5 are the two coastal ones. Additionally, for region 2, the predominant orientation angles were 0° and 45° ; for region 4, there was a slight preference for 90° ; and for region 1, a slight preference for 0° . Note that for all regions and durations, the angle of 135° had the lowest frequency and was around 10% to 15%. The aspect and angle histograms confirmed the need for accounting for anisotropy when analyzing storms.

In general, lower ARF values were observed compared to previous studies. Possible explanations of the differences between the ARF values calculated here and in previous studies include: (1) our values relate concurrent area to point precipitation, rather than annual mean values as TP-29 does; (2) precipitation ratios have a significant scatter as shown by [Asquith and Famiglietti \(2000\)](#); (3) our values account for the anisotropy of the precipitation field; and (4) our values were based on a 2-year set of spatially distributed radar-based precipitation estimates, rather than long records of point precipitation values.

ArcGIS_Storm is a geographical information system (GIS) tool developed as part of the project. It generates storm isohyets based on the ARF equations presented in [Chapter 4](#). ArcGIS_Storm is an add-in of the ESRI GIS software package ArcGIS.

8. REFERENCES

- Asquith, W.H., and J.S. Famiglietti (2000), *Precipitation areal-reduction factor estimation using an annual-maxima centered approach*, Journal of Hydrology 230 (1-2): 55-69.
- Bacchi, B., and R. Ranzi (1996), *On the derivation of the areal reduction factor of storms*, Atmospheric Research 42: 123-135.
- Bedient, B.P., B.C. Hobilt, D.C. Gladwell and B.E. Vieux (2000), *NEXRAD radar for flood prediction in Houston*, Journal of Hydrologic Engineering 5 (3): 269-277.
- Bedient, B.P., A. Holder, J. Benavides and B.E. Vieux (2003), *Radar-based flood warning system applied to tropical storm Allison*, Journal of Hydrologic Engineering 8 (6): 308-318.
- Carr, J.T. (1967), *The climate and physiography of Texas*, Texas Water Development Board, Report 53, 27 p.
- De Michele, C., N.T. Kottegoda and R. Rosso (2001), *The derivation of areal reduction factor of storm rainfall from its scaling properties*, Water Resources Research 37 (12): 3247-3252.
- Dixon, M., and G. Wiener (1993), *TITAN: Thunderstorm identification, tracking, analysis, and nowcasting – A radar-based methodology*, Journal of Atmospheric and Oceanic Technology 10 (6): 785-796.
- Durrans, S.R, L.T. Julian and M. Yekta (2002), *Estimation of depth-area relationships using radar-rainfall data*, Journal of Hydrologic Engineering 7 (5): 356-367.
- Eagleson, P.S. (1972), *Dynamics of flood frequency*, Water Resources Research 8 (4): 878-898.
- Frederick, R.H., V.A. Myers and E.P. Auciello (1977), *Storm depth-area relations from digitized radar returns*, Water Resources Research 13: 675-679.

- Fulton, R.A., J.P. Breidenbach, D.J. Seo and D.A. Miller (1998), *The WSR-88D rainfall algorithm*, Weather and Forecasting 13: 377-395.
- Giannoni, F., J.A. Smith, Y. Zhang and G. Roth (2003), *Hydrologic modeling of extreme floods using radar rainfall estimates*, Advances in Water Resources 26: 195-203.
- Mellor, D. (1996), *The modified turning bands (MTB) model for space-time rainfall. I. Model definition and properties*, Journal of Hydrology 175 (1-4): 113-127.
- Moon, J., R. Srinivasan and J.H. Jacobs (2004), *Stream flow estimation using spatially distributed rainfall in the Trinity River basin*, Transactions of the ASAE 47 (5): 1445-1451.
- Natural Environmental Research Council (1975), *Flood studies report*, Vol. 2, Institute of Hydrology, Wallingford.
- NWS (2002), *About Stage III data*, available online at http://www.nws.noaa.gov/oh/hrl/dmip/stageiii_info.htm as of 6/1/2005.
- NWS (2005), *Archive of River Forecast Center operational NEXRAD data*, available online at <http://dipper.nws.noaa.gov/hdsb/data/nexrad/nexrad.html> as of 8/26/2005.
- Ogden, F.L., and P.Y. Julien (1994), *Runoff model sensitivity to radar rainfall resolution*, Journal of Hydrology 158 (1-2): 1-18.
- Ogden, F.L., H.O. Sharif, S.U.S. Senarath, J.A. Smith, M.L. Baeck and J.R. Richardson (2000), *Hydrologic analysis of the Fort Collins, Colorado, flash flood of 1997*, Journal of Hydrology 228 (1-2): 82-100.
- Omolayo, A.S. (1993), *On the transposition of areal reduction factors for rainfall frequency estimation*, Journal of Hydrology 145 (1993): 191-205.
- Ott, R.L., and M.T. Longnecker (2001), *An introduction to statistical methods and data analysis*, Fifth Edition, Duxbury Press.

- Rigo, T., and M.C. Llasat (2002), *Analysis of convection in events with high amounts of precipitation using the metrological radar*, Proceedings of the 4th EGS Plinius Conference, Mallorca, Spain.
- Rodriguez-Iturbe, I., and J.M. Mejia (1974), *On the transformation of point rainfall to areal rainfall*, Water Resources Research 10 (4): 729-735.
- Seo, D.J. (2003), *Multi-sensor precipitation estimation*, NWSRFS International Workshop, Kansas City, October 21, 2003.
- Siriwardena, L., and P.E. Weinmann (1996), *Derivation of areal reduction factors for design rainfalls in Victoria*, Report 96/4, Cooperative Research Center for Catchment Hydrology, available online at <http://www.catchment.crc.org.au/pdfs/technical199604.pdf> as of 6/2/2005.
- Sivapalan, M., and G. Blöschl (1998), *Transformation of point rainfall to areal rainfall: Intensity-duration-frequency curves*, Journal of Hydrology 204 (1998): 150-167.
- Smith, J.A., M.L. Baeck, Y. Zhang and C. Doswell (2001), *Extreme rainfall and flooding from supercell thunderstorms*, Journal of Hydrometeorology 2 (5): 469-489.
- Srikathan, R. (1995), *A review of the methods for estimating areal reduction factors for design rainfalls*, Report 95/3, Cooperative Research Center for Catchment Hydrology, available online at <http://www.catchment.crc.org.au/pdfs/technical199503.pdf> as of 8/2/2005.
- USGS (1998), *Extreme precipitation depth for Texas, excluding the Trans-Pecos region*, Water Resources Investigations Report 98-4099, Austin, Texas.
- U.S. Weather Bureau (1957), *Rainfall intensity-frequency regime – Part 1: The Ohio Valley*, Technical Paper No. 29 (TP-29), Washington, D.C.
- U.S. Weather Bureau (1958a), *Rainfall intensity-frequency regime – Part 2: The Southeastern United States*, Technical Paper No. 29 (TP-29), Washington, D.C.
- U.S. Weather Bureau (1958b), *Rainfall intensity-frequency regime – Part 3: The Middle Atlantic Region*, Technical Paper No. 29 (TP-29), Washington, D.C.

- U.S. Weather Bureau (1959), *Rainfall intensity-frequency regime – Part 4: The Northeastern United States*, Technical Paper No. 29 (TP-29), Washington, D.C.
- U.S. Weather Bureau (1960), *Rainfall intensity-frequency regime – Part 5: The Great Lakes Region*, Technical Paper No. 29 (TP-29), Washington, D.C.
- U.S. Weather Bureau (1961), *Rainfall frequency atlas of the United States*, Technical Paper No. 40 (TP-40), Washington, D.C.
- U.S. Weather Bureau (1964), *Two- to ten-day precipitation for return periods of 2 to 100 years in the contiguous United States*, Technical Paper No 49 (TP-49), Washington, D.C.
- Vieux, B.E., and P.B. Bedient (2004), *Assessing urban hydrologic prediction accuracy through event reconstruction*, *Journal of Hydrology* 299 (3-4): 217-236.
- Vieux, B.E., and J.E. Vieux (2004), *Rainfall accuracy considerations using radar and rain gauge networks for rainfall-runoff monitoring*, in W. James, K.N. Irvine, E.A. McBean and R.E. Pitt (eds.), *Effective Modeling of Urban Water Systems*, Monograph 13, ISBN 0-9736716-0-2.
- Young, C.B., A.A. Bradley, W.F. Krajewski, A. Kruger and M.L. Morrissey (2000), *Evaluating NEXRAD multisensor precipitation estimates for operational hydrologic forecasting*, *Journal of Hydrometeorology* 1 (3): 241-254.